# Thermomechanical model for solidification and cooling simulation of Ni-based superalloy components

Carl Labergère, M. Long, Houssem Badreddine, N-T. Niane, D. Grange, Khemais Saanouni

# Thermomechanical model for solidification and cooling simulation of Ni-based superalloy components

C. Labergère [a*], M. Long[b], H. Badreddine[a], N-T. Niane[c], D.Grange[b], K. Saanouni[a]

[a)] ICD-LASMIS, University of Technology of Troyes/France

[b)] Safran Advanced Turbine Airfoils, a technology platform of Safran Tech, 171 Boulevard de Valmy, 92700 Colombes, France.

[c)] Safran Aircraft Engines, Material and Processes Laboratory, 171 Boulevard de Valmy, 92700 Colombes, France

**Abstract:** One of the challenges encountered in the industrialization of new single-crystal superalloys parts (like high-pressure turbine blades and vanes for aircraft engines) is to limit the mechanical stresses during the solidification and cooling of the metal. In order to accurately predict the viscoplastic flow as well as the thermo-mechanical behaviour of Ni-based superalloy during its cooling, in this study a thermodynamically-consistent thermo-elasto-viscoplastic model was developed. This model takes into account the solid-liquid transition occurring in the material during the cooling phase. This is done by introducing a compressible-type viscoplastic yield function based on appropriate equivalent stress depending on volume fraction of the solid phase formed by the propagation of dendrites inside the liquid phase of the material. This model was implemented in Abaqus/Standard© F.E. code and applied to the identification of material parameters of Ni-based superalloy using isothermal tensile-relaxation tests driven for different strain rates and temperatures. First, anisothermal tensile-compression test was simulated on a single integration point. A comparison of the experimental and numerical stress-strain response partially validate the model. Second, a benchmark test involving casting of a rectangular Ni-based superalloy bar in a sand mold was simulated and analyzed.

**Key Words**: Thermomechanics, coupling, multiphysics, Nickel alloy, cooling simulation, identification parameters, solidification, viscoplastiticty, casting

**Notations**

-First-rank tensor or vector: $x_i$ ,

* Corresponding author. Tel.: (+33) 3 25 75 96 47; fax: +...

*E-mail address:* carl.labergère@utt.fr

-Second-rank tensor: $x_{ij}$ ,

-Fourth-rank tensor: $x_{ijkl}$ ,

-Second-rank identity tensor : $\delta_{ij}$ ,

-Hydrostatic part of second-rank tensor $x_{ij}^{H}$

-Deviatoric part of second-rank tensor: $x_{ij}^{D}$ ,

-Inverse of second-rank tensor: $x_{ij}^{-1}$ ,

Time derivative of second-rank tensor : $\dot{x}_{ij}$ ,

## 1. Introduction

Single-crystal superalloys are creep-resistant materials particularly appropriate for making high pressure turbine blades and vanes for aircraft engines. (Pollock and Tin, 2006) give an extensive overview of the exceptional properties of such materials that make them particularly appropriate for such applications. They are processed by investment casting with a directional solidification, for an optimal control of the microstructure growth that is required for the fabrication of optimized single-crystal parts.

One of the challenges encountered in the industrialization of a new part is to limit the mechanical stresses during the solidification and cooling of the metal. As an example, excessive stresses at a high temperature are at the origin of recrystallized grains appearing during the post-processing heat-treatment and therefore leads to rejecting the parts. The origin of thermal stresses lies both in the thermal gradients and in the difference of thermal expansion coefficients between the metal and the ceramic mold (shell) and core. In particular, in high-pressure turbine blades, the ceramic core used to produce the internal cooling circuit induces additional stresses. This feature is supported by the work of (Li et al., 2015) who developed a thermomechanical model and used it to perform numerical analysis in order to identify the causes of plasticity during investment casting. The influence of the ceramic core in particular turned out to be more significant than the shell. Therefore, the metal after casting is plastically deformed and contains a high density of dislocations.

Consequently, modeling the solidification phenomenon is important because the latter can generate an undesirable state of stress in the component. (Pokorny et al., 2010) have proposed a compressible viscoplastic constitutive model of the mushy zone to simulate the stress state during a solidification. Initially, (Cocks, 1989) has proposed a criterion to model the behaviour of porous material based on homogenous RVE containing a spherical void. (Marin and McDowell, 1997) extended this work into a numerical framework to solve mechanical structure equilibrium problem with damage effects. (Galles and Beckermann, 2016) then had the idea to extend this work and adapted it to the cases of casting materials. The state of the casting part evolves continuously during its cooling. An effective stress based on solid metal volume fraction evolution is used to model the state evolution from the full liquid state to the full solid state throughout the semi-solid state. Instead, (Bellet et al ,2005; Zhang et al., 2019) proposed to model directly the interactions between the different phases (liquid/mush/solid) using a numerical method based on frontier definition. In this work, the constitutive model used for the solid phase was inspired from the work of (Martin et al, 1997). A set of macroscopic viscoplastic constitutive equations are preferred to simulate the behaviour of the solid phase because its calculation cost remains acceptable. In some cases, it is interesting to use microstructural models for the behaviour of single crystal (Fedelich, 2002). (Keshavarz and Gosh, 2013) also developed an activation energy-based crystal plasticity model for Ni-based single-crystal superalloys for simulating polycrystalline aggregates, while (Song and McDowell, 2012) proposed a crystal viscoplasticity model considering material's slip systems in order to capture its anisotropic response applied to Ni-base disk superalloy ME3 for temperatures around 700-800°C. The same type of approach has been used by (Cruzado et al.,

* Corresponding author. Tel.: (+33) 3 25 75 96 47; fax: +...

*E-mail address:* carl.labergère@utt.fr

2015) and (Cruzado et al. 2017) for studying polycrystalline materials (such as Inconel 718 or Rene 65) used for manufacturing structural gas turbine components (disks, rings, etc.). Nevertheless, the associated industrial process is forging and these materials are strengthened with $\gamma'$ and $\gamma$" precipitates, which largely differs from single-crystal superalloys such as AM1 used for casting ($\gamma'$precipitates only).

Therefore, plastic strain and residual stresses should be limited, by adjusting the parameters of the Bridgman directional solidification process or by modifying the shape of the parts. As this experimental step can be expensive and time consuming, numerical simulation of the process is useful to reduce the number of iterations until getting the optimized "virtual" process before its physical realization. An accurate numerical tool to simulate casting processes generally includes: (i) the thermal history resulting from conductive and radiative heat transfers over a large range of temperature (from approximately 700°C to 1500°C) , (ii) the mechanical properties of the mold and core, (iii) the contact condition between the mold and the metal part, an accurate mechanical model for the metal behavior from room temperature to melting temperature, (iv) and dedicated post-processing such as a recrystallization criterion based on the thermal and mechanical histories.

When coming to the simulation of the latter casting process, current numerical tools and constitutive models used by SAFRAN have shown severe limitations especially during the relaxation phase. The initial plastic strain phase is quite well predicted in terms of stress level, even though some deviation is observed at intermediate temperature when recrystallization is likely to occurs. As previously mentioned, both thermal and mechanical entire histories are important for the simulation of casting processes and structural default prediction e.g. the appearance of recrystallized grains during the solidification of a single-crystal.

The present work aims at developing a modified behaviour model adapted from the classical Voce isotropic hardening model with an additional modified Norton-Hoff potential. One interesting feature of this model is the possibility to take into account liquid-mushy-solid transitions that are often neglected in solidification simulations. Its numerical implementation in the Abaqus/Standard© environment is then presented. Elementary validation of the present methodology is then conducted on both isothermal and anisothermal tests of simple specimens from room temperature to 1200°C for two typical strain rates. A FEM cooling model of a rectangular Ni-based superalloy bar in a sand mold is simulated and analyzed. Particular care has been given to the well description of casting process conditions in terms of temperature and strain rate fields.

## 2. Thermo-elasto-visco-plastic constitutive model

### Theoretical aspects

A semi-solid viscoplastic behavior model is developed based on a well-known isotropic model with only isotropic hardening. Based on the work of (Galles and Beckermann, 2016), the semi-solid state created during solidification is modeled as a compressible porous material where the stress tensor depends on the pressure as follows:

$$\tilde{\sigma}_{ij} = g_s \sigma_{ij}^s + (1 - g_s) p_l \delta_{ij} \qquad (1)$$

where $g_s$ is the solid state volume fraction varying between 1 and 0, i.e. $\tilde{\sigma}_{ij} = \sigma_{ij}^s$ is the stress tensor inside the full solid state ( $g_s$ =1) and $\tilde{\sigma}_{ij} = p_l$ (hydrostatic pressure) inside the full liquid state.

An additive decomposition of the total strain rate tensor into elastic, viscoplastic and thermal parts is considered:

$$\begin{aligned} \dot{\varepsilon}_{ij} &= \dot{\varepsilon}_{ij}^e + \dot{\varepsilon}_{ij}^{vp} + \dot{\varepsilon}_{ij}^{th} \\ \varepsilon_{ij}^{th} &= \alpha_T (T - T_{th}) \delta_{ij} \end{aligned} \qquad (2)$$

where $\alpha_T$ is the thermal expansion coefficient which is temperature-dependent function and $T_{th}$ is the reference temperature.

In the present work, the following assumptions are adopted:

- Reversible (elastic) strains are negligible compared to irreversible inelastic (plastic or viscoplastic) strain. In this case, we can rigorously consider the additive decomposition of the total strain rate tensor.
- The strain-hardening is introduced phenomenologically and limited to the isotropic hardening.
- A unified formulation is adopted to deal with an elastoplastic (time-independent) and elasto-viscoplastic (time-dependent) behaviour models.
- Despite the single crystal aspect of the material, fully isotropic behaviour is assumed (Elastic and plastic anisotropies are neglected).
- The recovery phenomenon is not considered.
- The dynamic recrystallization phenomenon is not directly modeled, but its softening effect on the stress-strain response is introduced by the possibility of accepting negative isotropic strain-hardening.
- The updated Lagrangian formalism is used.

The yield function $f$ is chosen to describe the viscoplastic behaviour of the Ni-based superalloy, in the stress space. The equivalent stress norm is composed on both first and second stress invariants:

$$f = \sigma_{eq} - h_3(g_s)\sigma_s \leq 0 \qquad (3)$$

where

$\sigma_{eq} = \sqrt{h_1(g_s) q_s^2 + h_2(g_s) p_s^2}$ is a quadratic equivalent stress

$q_s^2\left(\tilde{\sigma}_{ij}\right)=\frac{3}{2}\tilde{\sigma}_{ij}^D\tilde{\sigma}_{ij}^D$ is the second invariant of the effective stress with $\tilde{\sigma}_{ij}^D$ is the deviatoric part of the Cauchy stress tensor,

$p_s\left(\tilde{\sigma}_{ij}\right)=tr\left(\tilde{\sigma}_{ij}\right)/3=\tilde{\sigma}_{ii}/3$ is the first invariant of the effective stress,

$\sigma_s$ is the isotropic hardening stress,

$h_i(g_s)\{i=1,2,3\}$ are functions of the metal solid volume fraction.

Several authors as (Cocks, 1989; Marin and McDowell, 1997; Michel and Suquet, 1992) initially used this form of criterion to model the behaviour of porous continua to account for the porosity generated by cavitation during ductile damage.

When the part is completely solidified the volume fraction converge to $g_s$=1, and classical von Mises stress norm is recovered when functions $h_1$, $h_2$ and $h_3$ take the following values:

$$h_1(1)=1,\ h_2(1)=0,\ h_3(1)=1 \qquad (4)$$

The formulation of the proposed behaviour model is formulated on the framework of viscoplasticity known as "viscoplastic potential" based on the work of (Perzyna, 1966; Lemaitre and Chaboche, 1985; Saanouni, 2013; Badreddine et al.; 2016) have then analyzed the contribution of a “viscoplastic potential” to viscoplasticity with damage in the framework of classical thermodynamics of irreversible processes with state variables. For example, (Issa et al., 2012; Meng et al., 2014) specifically used this way to introduce viscous behaviour for the simulation of a machining operation and forging processes.

The proposed viscoplastic potential is a modification of the Norton-Hoff potential:

$$\Omega\left(\tilde{\sigma}_{ij},\varepsilon_{eq}^{vp},T\right)=\dot{\varepsilon}_0\frac{K_v\left(\varepsilon_{eq}^{vp},T\right)}{\left(\frac{1}{n_T}+1\right)}\left(\frac{f\left(\tilde{\sigma}_{ij},\varepsilon_{eq}^{vp},T\right)}{h_3(g_s)K_v\left(\varepsilon_{eq}^{vp},T\right)}\right)^{\frac{1}{n_T}+1} \qquad (5)$$

where $n_T$ and $K_v\left(\dot{\varepsilon}^{eq},T\right)$ are classical viscosity parameters of Norton-Hoff type with $K_v$ is positive function of the equivalent viscoplastic strain rate defined by $\dot{\varepsilon}_{eq}^{vp}=(2/3)\left(\dot{\varepsilon}_{ij}^{vp}:\dot{\varepsilon}_{ij}^{vp}\right)$ and the absolute temperature $T$. finally, $\dot{\varepsilon}_0$ is a reference strain rate independent of the temperature.

In this viscoplasticity framework, the viscoplastic strain rate tensor is calculated by deriving the flow potential with respect to the effective stress tensor:

$$\dot{\varepsilon}_{ij}^{vp}=\frac{\partial\Omega}{\partial\tilde{\sigma}_{ij}}=\frac{\partial\Omega}{\partial f}\frac{\partial f}{\partial\tilde{\sigma}_{ij}}=\dot{\lambda}_{vp}n_{ij} \qquad (6)$$

where $n_{ij} = \partial f / \partial \tilde{\sigma}_{ij}$ is the normal to the viscoplastic yield surface defining the direction of the viscoplastic flow, and the the scalar $\dot{\lambda}_{vp}$ acts as a viscoplastic "multiplier" defining the amount of viscoplastic strain rate where $\dot{\lambda}_{vp} = \dot{\varepsilon}_{eq}^{vp} = \dfrac{\partial \Omega}{\partial f} = \dot{\varepsilon}_0 \left( \dfrac{f\left(\tilde{\sigma}_{ij}, \varepsilon_{eq}^{vp}, T\right)}{h_3(g_s) K_v\left(\varepsilon_{eq}^{vp}, T\right)} \right)^{\frac{1}{n_T}}$. In the previous equation, we can draw $f$ as a function of $\dot{\lambda}_{vp}$ or $\dot{\varepsilon}_{eq}^{vp}$

$$f = \sqrt{h_1(g_s) q_s^2 + h_2(g_s) p_s^2} - h_3(g_s)\sigma_s\left(\varepsilon_{eq}^{vp}, T\right) = h_3(g_s) K_v\left(\varepsilon_{eq}^{vp}, T\right)\left(\frac{\dot{\varepsilon}_{eq}^{vp}}{\dot{\varepsilon}_0}\right)^{n_T} \quad (7)$$

This equation expresses the viscoplastic yield surface according to Perzyna's work:

$$f_{vp}\left(\tilde{\sigma}_{ij}, \varepsilon_{eq}^{vp}, \dot{\varepsilon}_{eq}^{vp}, T\right) = f\left(\tilde{\sigma}_{ij}, \varepsilon_{eq}^{vp}, T\right) - h_3 \sigma_{vp}\left(\varepsilon_{eq}^{vp}, \dot{\varepsilon}_{eq}^{vp}, T\right) = 0 \quad (8)$$

wherein $\sigma_{vp}$ is the viscous stress defined by

$$\sigma_{vp}\left(\varepsilon_{eq}^{vp}, \dot{\varepsilon}_{eq}^{vp}, T\right) = K_v\left(\varepsilon_{eq}^{vp}, T\right)\left(\frac{\dot{\varepsilon}_{eq}^{vp}}{\dot{\varepsilon}_0}\right)^{n_T} \quad (9)$$

The isotropic hardening stress $\sigma_s$ and the $K_v$ module are nonlinear functions of Voce type given by:

$$\begin{aligned} \sigma_s(\varepsilon_{eq}^{vp}, T) &= \sigma_T^e + A_T\left(1 - e^{-b_T \varepsilon_{eq}^{vp}}\right) \\ K_v(\varepsilon_{eq}^{vp}, T) &= K_{vT}\left(1 - e^{-b_{vT} \varepsilon_{eq}^{vp}}\right) \end{aligned} \quad (10)$$

where $\sigma_T^e$ is the initial yield stress, $A_T$ is the isotropic hardening modulus, $b_T$ is the nonlinearity coefficient of the isotropic hardening, $K_{vT}$ is the viscosity modulus, and $b_{vT}$ is the nonlinearity coefficient of the viscous hardening. All these parameters are function of the absolute temperature $T$.

Only in the case of Norton Hoff viscoplastic potential, (Cocks, 1989) propose the weighting functions $h_i$, used to build the specific stress norm for the yield surface $f$. (Michel and Suquet, 1992) then generalized this work and proposed several weight functions related to different viscoplastic potential. These functions are based on the definition of a model relying on closed-form solutions for a hydrostatic tensile loading path applied to the outer surface of a hollow sphere in the case of viscous and incompressible matrix of the porous material.

$$\begin{cases} h_1(g_s) = 1 + \frac{2}{3}(1 - g_s^*) \\ h_2(g_s) = \dfrac{1}{2}\left(\dfrac{1 - g_s^*}{2 - g_s^*}\right)\dfrac{1}{1 + n_{T_{coh}}} \\ h_3(g_s) = g_s^{*1/(1+n_{T_{coh}})} \end{cases} \quad (11)$$

with $g_s^* = \left(g_s - g_s^{coh}\right) / \left(g_s^{coal} - g_s^{coh}\right)$ where $g_s^{coh}$ corresponds to the solid metal volume fraction at the coherence temperature $T_{coh}$ and $g_s^{coal}$ corresponds to the solid volume fraction at the coalescence temperature $T_{coal}$. In practice, the values of these parameters are approximately $g_s^{coal} = 0.9$ and $g_s^{coh} = 0.5$. The variable $n_{T_{coh}}$ is the last value identified at the highest temperature used in the material characterization tests. Figure 1 gives an example of the evolution of these functions drawn for $n_{T_{coh}} = 0.26$.

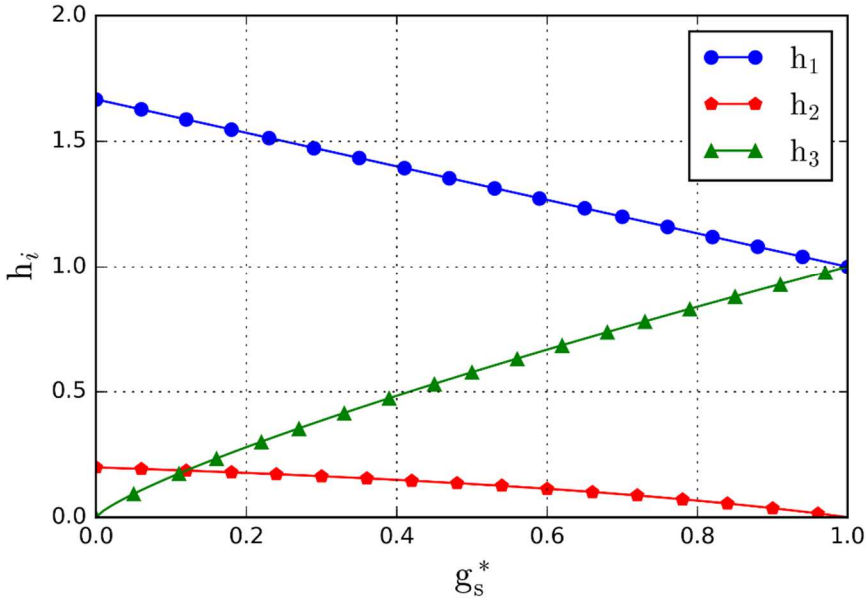


*Figure 1: Evolution of the function* $h_1(g_s), h_2(g_s) et h_3(g_s)$ *for* $n_{T_{coh}} = 0.26$

We have chosen this form of the threshold function associated to the yield function $f^{vp}\left(\tilde{\sigma}_{ij}, \varepsilon_{eq}^{vp}, \dot{\varepsilon}_{eq}^{vp}, T\right)$ for three reasons:

-It is easier to isolate the viscous stress $\sigma_{vp}\left(\varepsilon_{eq}^{vp}, \dot{\varepsilon}_{eq}^{vp}, T\right)$ and identify its parameters with the relaxation test.

-this form seems better to predict the stress-strain response as well as the evolution of the stress vs time during the relaxation phase.

-The viscoplastic potential is taken from the work of (Cocks, 1989 and Michel and Suquet, 1992). This viscoplastic potential is coherent with the Norton-Hoff form when we introduce solid fraction functions $h_1$, $h_2$ and $h_3$.

During the cooling phase, when the part temperature changes from $T_{coh}$ to $T_{coal}$, the state relationship between the stress tensor and the elastic strain tensor changes as follows:

$$\tilde{\sigma}_{ij} = 2\mu_e(g_s, \mathrm{T})\varepsilon_{ij}^{eD} + \frac{K_e(g_s, \mathrm{T})}{3} tr(\varepsilon_{kl}^{e})\delta_{ij} \qquad (12)$$

where $\mu_e(g_s)=\frac{E(g_s,\mathrm{T})}{2(1+\nu(g_s))}$ is the shear effective modulus and $K_e(g_s,\mathrm{T})=\frac{E(g_s,\mathrm{T})}{(1-2\nu(g_s))}$ is the effective hydrostatic compression modulus. $E(g_s,\mathrm{T})$ and $\nu(g_s)$ being respectively the effective Young's and Poisson's ratio of the pasty material as a function of temperature and solid metal volume fraction. The expressions of theses elasticity parameters are defined based on work of (Galles and Beckerman, 2016):

$$E(g_s,\mathrm{T})=(1-g_s)E_l+E_s(T)\left(\frac{g_s-g_s^{coh}}{1-g_s^{coh}}\right)=\begin{cases}E_s, & g_s=1\\ E_l, & g_s\le g_s^{coh}\approx 0.5\end{cases} \quad (13)$$

$$\nu(g_s)=\nu_0+\frac{g_s-g_s^{coh}}{1-g_s^{coh}}(\nu_s-\nu_0)=\begin{cases}\nu_s=0.3, & g_s=1\\ \nu_0=0.14, & g_s=g_s^{coh}\approx 0.5\end{cases} \quad (14)$$

$E_l$ and $E_s(T)$ are respectively the Young's moduli in liquid metal phase and the solid metal phase. The module $E_l$ is chosen low enough to have almost no stress in the liquid phase. The Poisson's ratios coefficients $\nu_0$ and $\nu_s$ characterize the liquid metal and solid metal phases respectively.

***Identification of the different material parameters***

SAFRAN's laboratories have performed tensile/relaxation tests on cylindrical specimens under various controlled total strain rates $\dot{\varepsilon}_{eq}$ and temperatures $T$. Only the solid metal behaviour is characterized. The maximum temperature is then lower than the solidus temperature.

Figure 2 shows the evolution of uniaxial stress vs the time during a typical tensile/relaxation test. The path A to B corresponds to an isothermal homogeneous tensile test. The path B to C state corresponds to the relaxation test for which the recovery of the reversible viscous stress $\sigma_{vp}$ for more or less long time is clearly shown.

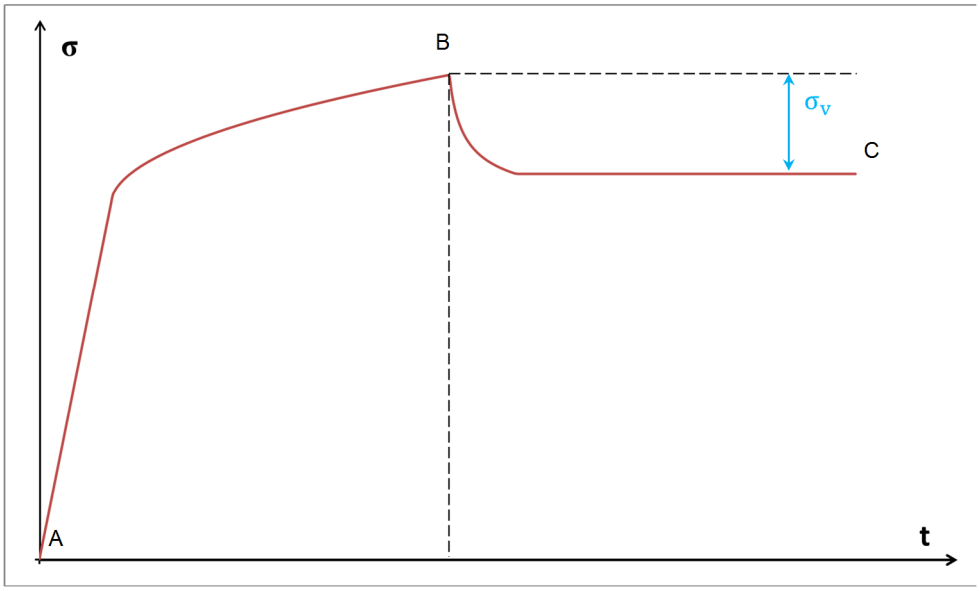

*Figure 2: Uniaxial stress vs time response associated to a tensile/relaxation test*

Initially, relaxation tests are used to identify only the viscous stress parameters $K_{vT}$ and $n_T$ for a given temperature $T$. If $\varepsilon_{eqB}^{vp}$ is the cumulative viscoplastic strain in the specimen after the tensile test, we try to find parameters $K_v^B = K_v\left(\varepsilon_{eqB}^{vp}, T\right)$ and $n_T$ that minimize the difference between the experimental value of the viscous stress and the viscous stress given by the behaviour model for different values of total strain rate $\dot{\varepsilon}_j^{eq}$ :

$$R_{\min 1} = \min_{K_v^B, n_T}\left(\sum_{j=1}^{M}\left(\sigma_v - K_v^B\left(\frac{\dot{\varepsilon}_{eqj}^{vp}}{\dot{\varepsilon}_0}\right)^{n_T}\right)^2\right) \qquad (15)$$

where $M$ is the number of experimental tests for the same temperature $T$ but whose total strain rate $\dot{\varepsilon}_j^{eq}$ is varied.

For the remaining parameters of the behaviour model, experimental stress/strain hardening curves $\sigma_{\exp}$ at different temperatures and strain rates are used.

$$R_{\min 2} = \min_{\sigma_T^e, Q_T, b_T, \beta_T}\left(\sum_{j=1}^{M}\frac{1}{N}\sum_{i=1}^{N}\left(\sigma_{\exp}\left(\varepsilon_{eq\,i}^{vp}, \dot{\varepsilon}_{eqj}^{vp}, T\right) - \sigma_{num}\left(\varepsilon_{eq\,i}^{vp}, \dot{\varepsilon}_{eqj}^{vp}, T\right)\right)^2\right)$$

$$with\ \sigma_{num}\left(\varepsilon_{eq\,i}^{vp}, \dot{\varepsilon}_{eqj}^{vp}, T\right) = \sigma_T^e + A_T\left(1 - e^{-b_T\varepsilon_{eq\,i}^{vp}}\right) + \underbrace{\left(\frac{K_v^B}{1 - e^{-\beta_T\varepsilon_{eqN}^{vp}}}\right)}_{K_{vT}}\left(1 - e^{-\beta_T\varepsilon_{eq}^{vp}}\right)\left(\frac{\dot{\varepsilon}_{eqj}^{vp}}{\dot{\varepsilon}_0}\right)^{n_T} \qquad (16)$$

N being the number of discretization of the cumulative plastic deformation such that $\varepsilon_{eqi}^{vp} = \frac{\varepsilon_{eqB}^{vp}}{N} i$

A Levenberg-Marquardt algorithm (Marquardt, 1963) was used to minimize the cost functions $R_{min1}$ and $R_{min2}$ and calculate the optimal parameters

## 3. Numerical aspects

The use of the proposed model needs an efficient local integration scheme in order to integrate the complete set of the ordinary differential equations Eq.(2) to Eq.(10). Each applied loading path is discretized into several load increments typically defined as [$t_n$, $t_{n+1} = t_n + \Delta t$ ] with $\Delta t$ is the varying time step. The fully coupled thermomechanical problem is solved over the time interval under anisothermal condition (i.e. $T_{n+1} = T_n + \Delta T$ ) in order to obtain the mechanical variables at $t_{n+1}$. These fully coupled thermomechanical constitutive equations presented above have been implemented into Abaqus/Standard© using the user-defined subroutine UMAT. During the resolution of the mechanical problem under the

anisothermal conditions with known homogeneous temperature distribution, the mechanical variables at each integration point are computed at the time $t_{n+1}$ assuming that all the state variables are known at $t_n$. Since the constitutive equations above have the general form of first-order ordinary differential equations, their numerical integration can be performed by combining the backward Euler purely implicit scheme. Using this scheme, we can obtain the following discretization of the kinematic strain variables:

Total strain tensor :

$$\varepsilon_{ijn+1} = \varepsilon_{ijn} + \Delta t\dot{\varepsilon}_{ijn+1} = \varepsilon_{ijn} + \Delta\varepsilon_{ij} \qquad (17)$$

Elastic strain tensor :

$$\varepsilon^e_{ijn+1} = \varepsilon^e_{ijn} + \Delta t\dot{\varepsilon}^e_{ijn+1} = \varepsilon^e_{ijn} + \Delta\varepsilon^e_{ij} \qquad (18)$$

Thermal strain tensor:

$$\varepsilon^{th}_{ijn+1} = \varepsilon^{th}_{ijn} + \Delta\varepsilon^{th}_{ij} = \varepsilon^{th}_{ijn} + \Big[\ \alpha_{T_{n+1}}(T_{n+1} - T_{ref}) - \alpha_{T_n}(T_n - T_{ref})\Big]\delta_{ij} \qquad (19)$$

Viscoplastic strain tensor:

$$\begin{aligned} \varepsilon^{vp}_{ijn+1} &= \varepsilon^{vp}_{ijn} + \Delta t\dot{\varepsilon}^{vp}_{ijn+1} = \varepsilon^{vp}_{ijn} + \Delta\varepsilon^{vp}_{ij} \\ \Delta\varepsilon^{vp}_{ij\,n+1} &= \Delta\varepsilon^{vp}_{eqn+1} n_{ijn+1} = \frac{\Delta\varepsilon^{vp}_{eqn+1}}{\sigma^{eq}_{n+1}}\left(\tfrac{3}{2}h_1(g_{sn+1})\tilde{\sigma}^D_{ijn+1} + h_2(g_{sn+1})tr(\tilde{\sigma}_{kl\,n+1})\delta_{ij}\right) \end{aligned} \qquad (20)$$

where $\Delta\varepsilon^{vp}_{eqn+1}$ denotes the increment of the accumulated viscoplastic strain .

Decomposition of the total strain increment:

$$\Delta\varepsilon_{ij} = \Delta\varepsilon^e_{ij} + \Delta\varepsilon^{vp}_{ij} + \Delta\varepsilon^{th}_{ij} = \Delta\varepsilon_{ij}\,' + \Delta\varepsilon^{th}_{ij} \qquad (21)$$

where $\Delta\varepsilon_{ij}\,'$ denotes the purely mechanical strain increment.

$$\Delta\varepsilon_{ij}\,' = \Delta\varepsilon_{ij} - \Delta\varepsilon^{th}_{ij} = \Delta\varepsilon^e_{ij} + \Delta\varepsilon^{vp}_{ij} \qquad (22)$$

Cauchy stress tensor:

$$\tilde{\sigma}_{ij\,n+1} = \tilde{\sigma}_{ij\,n} + C^e_{ijkl}(g_{sn+1}, T_{n+1})\Delta\varepsilon^e_{kl} = \tilde{\sigma}_{ij\,n} + C^e_{ijkl}(g_{sn+1}, T_{n+1})(\Delta\varepsilon_{kl}\,' - \Delta\varepsilon^{vp}_{ij}) \qquad (23)$$

where $C^e_{ijkl}(g_{sn+1}, T_{n+1})$ is the effective elastic forth rank operator which is function of the solid volume fraction and the temperature.

The well-known elastic prediction and viscoplastic correction scheme is used to determine all the mechanical fields over the time increment. In the trial elastic step, we suppose that all internal variables remain unchanged giving $\Delta\varepsilon^{vp}_{ij} = 0$ leading to the following expression of the trial stress tensor:

$$\tilde{\sigma}^{*}_{ij\,n+1} = \tilde{\sigma}_{ij\,n} + C^{e}_{ijkl}(g_{sn+1}, T_{n+1})\Delta\varepsilon^{e*}_{kl} = \tilde{\sigma}_{ij\,n} + C^{e}_{ijkl}(g_{sn+1}, T_{n+1})\Delta\varepsilon_{kl}'$$
$$\tilde{\sigma}^{*}_{ij\,n+1} = \tilde{\sigma}_{ij\,n} + 2\mu_e(g_{sn+1}, T_{n+1})\Delta\varepsilon^{D}_{ij}' + \frac{K_e(g_{sn+1}, T_{n+1})}{3} tr(\Delta\varepsilon_{ij}')\delta_{ij} \qquad (24)$$

The viscoplastic yield function Eq.(7) writes, for this trial state:

$$f^{*}_{n+1} = \sigma^{eq*}_{n+1}(\tilde{\sigma}^{*}_{ij\,n+1}, g_{sn+1}) - h_3(g_{sn+1})\sigma_s(\varepsilon^{vp}_{eqn}, T_{n+1})$$
$$\sigma_s(\varepsilon^{vp}_{eqn}, T_{n+1}) = A_{T_{n+1}}(1 - Exp(-b_{T_{n+1}}\varepsilon^{vp}_{eqn})) + \sigma^{e}_{T_{n+1}} \qquad (25)$$

If $f^{*}_{n+1} \le 0$ so the loading increment is purely elastic and the solution of the current step : $\tilde{\sigma}_{ijn+1} = \tilde{\sigma}^{*}_{ijn+1}$, $\varepsilon^{vp}_{ij\,n+1} = \varepsilon^{vp}_{ij\,n}$, $\dot{\varepsilon}^{vp}_{ij\,n+1} = \dot{\varepsilon}^{vp}_{ij\,n}$,

If $f_{n+1} > 0$ so the loading increment is elasto-viscoplastic and a viscoplastic correction should be performed on trial stress based on the normal return mapping algorithm

The expression of the stress during the step of viscoplastic correction is given by:

$$\tilde{\sigma}_{ij\,n+1} = \tilde{\sigma}^{*}_{ij\,n+1} - \left[ 2\mu_e\Delta\varepsilon^{vpD}_{ijn+1} + \frac{K_e}{3} tr(\Delta\varepsilon^{vp}_{ijn+1})\delta_{ij} \right]$$
$$\Delta\varepsilon^{vp}_{ij\,n+1} = \Delta\varepsilon^{vp}_{eqn+1} n_{ijn+1} = \frac{\Delta\varepsilon^{vp}_{eqn+1}}{\sigma^{eq}_{n+1}}\left(\frac{3}{2} h_1\tilde{\sigma}^{D}_{ijn+1} + h_2 tr(\tilde{\sigma}_{kl\,n+1})\delta_{ij}\right) \qquad (26)$$
$$\tilde{\sigma}_{ij\,n+1} = \tilde{\sigma}^{*}_{ij\,n+1} - \frac{\Delta\varepsilon^{vp}_{eqn+1}}{\sigma^{eq}_{n+1}}\left[ 3\mu_e h_1\tilde{\sigma}^{D}_{ijn+1} + K_e h_2 tr(\tilde{\sigma}_{kl\,n+1})\delta_{ij}) \right]$$

where the term $2\mu_e\Delta\varepsilon^{vpD}_{ijn+1} + \frac{K_e}{3} tr(\Delta\varepsilon^{vp}_{ijn+1})\delta_{ij}$ constitutes the viscoplastic correction. The stress state defined by Eq.(26) shall verify the viscoplastic criterion defined by Eq(8) :

$$f_{vp\,n+1} = \sigma^{eq}_{n+1}(\tilde{\sigma}_{ij\,n+1}, g_{sn+1}) - h_3(g_{sn+1})\sigma_{sn+1}(\varepsilon^{vp}_{eqn+1}, T_{n+1}) - h_3(g_{sn+1})\sigma_{vpn+1}(\varepsilon^{vp}_{eqn+1}, \dot{\varepsilon}^{vp}_{eqn+1}, T_{n+1}) = 0$$
$$\sigma_{sn+1}(\varepsilon^{vp}_{eqn+1}, T_{n+1}) = \sigma^{e}_{T}(T_{n+1}) + A_{Tn}(T_{n+1})(1 - Exp(-b_{Tn+1}(T_{n+1})\varepsilon^{eq}_{n})) \qquad (27)$$
$$\sigma^{vp}_{n+1}(\varepsilon^{vp}_{eqn+1}, \dot{\varepsilon}^{vp}_{eqn+1}, T_{n+1}) = K_{vT}(T_{n+1})(1 - Exp(-b_{vT}(T_{n+1})\varepsilon^{vp}_{eqn}))\left(\frac{\Delta\varepsilon^{vp}_{eqn+1}}{\Delta t\dot{\varepsilon}_0}\right)^{n_T(T_{n+1})}$$

Eq. (27) form a highly nonlinear system which is uniquely function of accumulated viscoplastic strain increment $\Delta\varepsilon^{vp}_{eqn+1}$ since $T_{n+1}$ is known. The resolution is reduced to the resolution by the Newton-Raphson method of the equation Eq.(11) depending on the only variable $\Delta\varepsilon^{vp}_{eqn+1}$.

$$f^{(k+1)}_{vp\,n+1} + \frac{\partial f_{vp\,n+1}}{\partial\Delta\varepsilon^{vp}_{eqn+1}}\delta\Delta\varepsilon^{vp(k)}_{eqn+1} = 0 \Rightarrow \delta\Delta\varepsilon^{vp(k)}_{eqn+1} = -\frac{f^{(k+1)}_{vp\,n+1}}{\partial f^{(k)}_{vp\,n+1} / \partial\Delta\varepsilon^{vp}_{eqn+1}} \qquad (28)$$
$$\Delta\varepsilon^{vp(k+1)}_{eqn+1} = \Delta\varepsilon^{vp(k)}_{eqn+1} + \delta\Delta\varepsilon^{vp(k)}_{eqn+1}$$

The calculation of the term $\partial f^{(k)}_{vp\,n+1} / \partial\Delta\varepsilon^{vp}_{eqn+1}$ is given in Appendix 1.

The ABAQUS® implicit solver requires the calculation of the tangent operator which plays an important role in the convergence of the iterative process of solving the global equilibrium problem. This operator must be determined consistently with the calculation of the stress at the end of the time step. The expression of this consistent operator is given as follows:

$$\Delta\tilde{\sigma}_{ij} = C_{ijkl}\Delta\varepsilon_{kl} \tag{29}$$

The expression of the tangent operator $C_{ijkl}$ is given in Appendix 2.

The different steps of the integration algorithm are given in Figure 3 and explained in the following:

1-For $t_n$=0 initialization of all state variables,

2- For each given time increment $\Delta t$, thermal and mechanical increment ($\Delta T$ and $\Delta\varepsilon_{ij}$) are imposed,

3-test if $T_{n+1} = T_n + \Delta T > T_{coh}$ :

3-1.then the material is in the liquid phase and the behavior is considered as thermo-elastic with very small Young's modulus and Poisson coefficient $\nu \approx 0.5$ (incompressible material),

3-2. we pass to the following time increment n: =n+1,

4-if not, the material is in solid-mushy phase and we calculate the elastic trial stress,

5-Test if the trial criterion $f^*_{n+1} \leq 0$

5-1. then the loading increment is purely thermo-elastic,

5-2. the stress tensor is updated $\tilde{\sigma}_{ijn+1} = \tilde{\sigma}^*_{ijn+1}$,

5-3. plastic variable remains unchanged , $\varepsilon^{vp}_{ij\,n+1} = \varepsilon^{vp}_{ij\,n}, \dot{\varepsilon}^{vp}_{ij\,n+1} = \dot{\varepsilon}^{vp}_{ij\,n}$,

5-4. we pass to the following time increment n: =n+1,

6- if not, the loading increment is thermo-elasto-viscoplastic and viscoplastic correction will be done with Newton-Raphson iterative method:

6-1. for iteration k, calculate :viscoplastic strain $\varepsilon^{vp(k)}_{ij\,n+1}$, strain rate $\dot{\varepsilon}^{vp(k)}_{ij\,n+1}$ and stress $\tilde{\sigma}^{(k)}_{ijn+1}$,

6-2. calculate the viscoplastic criterion $f^{(k)}_{vp\,n+1}$,

6-3. Test if the criterion $\left|\frac{f^{(k)}_{vp\,n+1}}{f^{(0)}_{vp\,n+1}}\right| < \text{Tol} = 1.e^{-6}$ then

6-3-1.the N-R method converged to the correct solution,

6-3-2.we pass to the following time increment n: =n+1,

6-4. If not :

6-4-1. calculate the increment of accumulated viscoplastic strain,

6-4-2. update the iteration k:=k+1,

6-4-3. Test if the number of iteration max is not reached $k<n_{max}=100$ then go to step 6-2,

6-4-4. If not, the number of iteration max is reached without convergence so the loading increment is canceled and the time increment is reduced and return to step1.

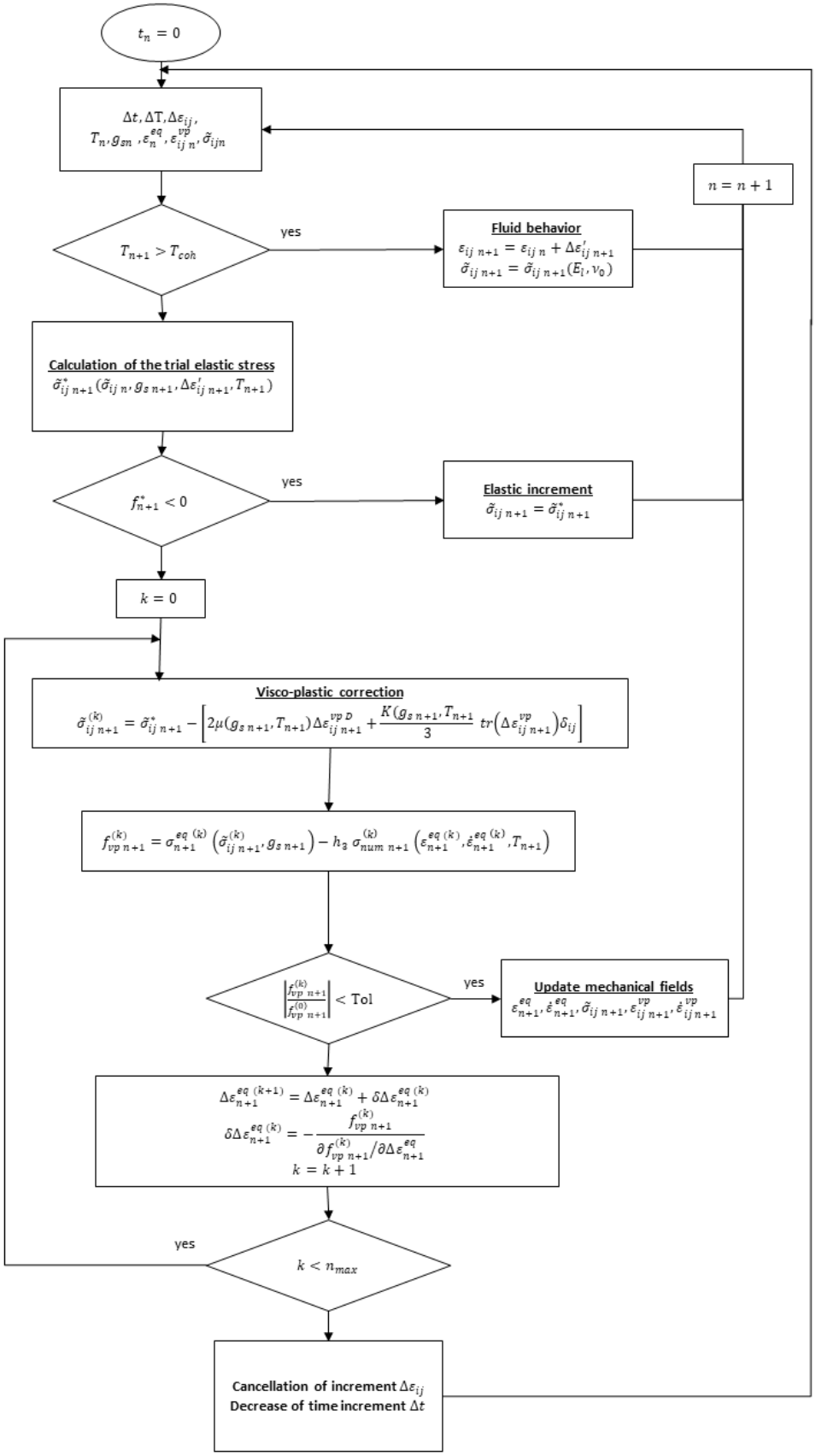


*Figure 3. Integration algorithm of the developed thermoviscoelastoplastioc model.*

## 4. Experimental characterization of the studied materials and Identification procedure of material parameters

**Material and experimental conditions**

The tested material is a single crystal type AM1 – the nominal composition of which is reported in Table 1. This crystal is a face-centered cubic Ni-based γ-matrix containing a high volume fraction (65-70% at room temperature) of $Ni_3Al$-type γ‘ phase submicronic strengthening precipitates. The thermal material parameters of AM1 are listed in Table 2.

| Alloy | Ni | Co | Cr | Mo | W | Al | Ti | Ta |
|---|---|---|---|---|---|---|---|---|
| AM1 | base | 7.8 | 6.5 | 2 | 5.7 | 5.2 | 1.1 | 7.9 |

*Table 1. Nominal composition of AM1 (wt%)*

| Specific heat Cp ($J.kg^{-1}.°C^{-1}$) | Conductivity k ($W.m^{-1}.°C^{-1}$) | Solidus temperature Ts (°C) | Coalescence temperature $T_{coal}$ (°C) | Coherence temperature $T_{coh}$ (°C) | Liquidus temperature $T_l$ (°C) |
|---|---|---|---|---|---|
| 931. | 180. | 1255. | 1269. | 1300. | 1320. |

*Table 2. AM1's thermal material parameters (courtesy of Safran Aircraft Engines)*

Figure 4 shows the evolution of solid fraction ($g_s$) vs temperature for AM1 ($T<T_s=1255°C \rightarrow g_s=1$; $T>T_l=1320°C \rightarrow g_s=0$ measured by differential thermal analysis (DTA, DSC). Ts and Tl are respectively the solidus and liquidus temperature of AM1 Ni-based superalloy. In this figure are given also the coherence $T_{coal}$ =1269°C and coalescence $T_{coh}$ =1300°C temperatures associated to their respective values of volume fractions $g_s^{coal}=0.9$ and $g_s^{coh}=0.5$ (Galles & Beckermann, 2016) defined in the evolutions of functions $h_i(g_s)\{i=1,2,3\}$ given in Eq.(11).

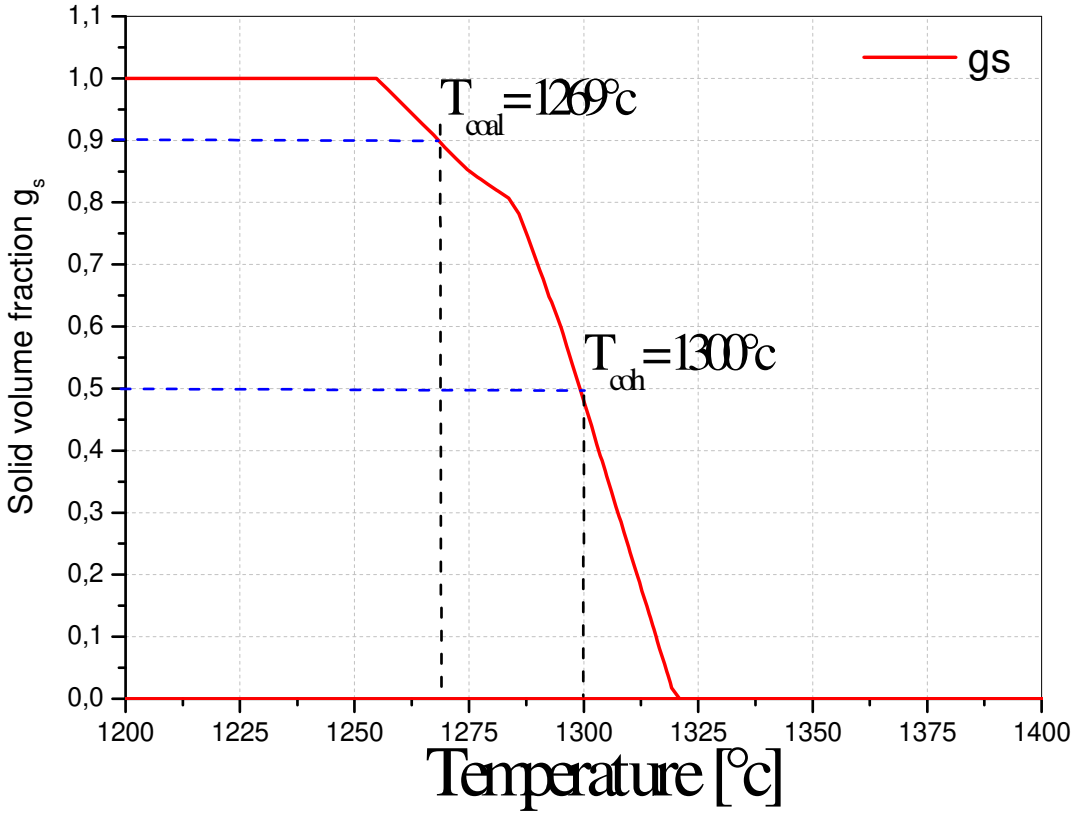


*Figure 4. Solid volume fraction vs temperature of AM1 (courtesy of Safran Aircraft Engines)*

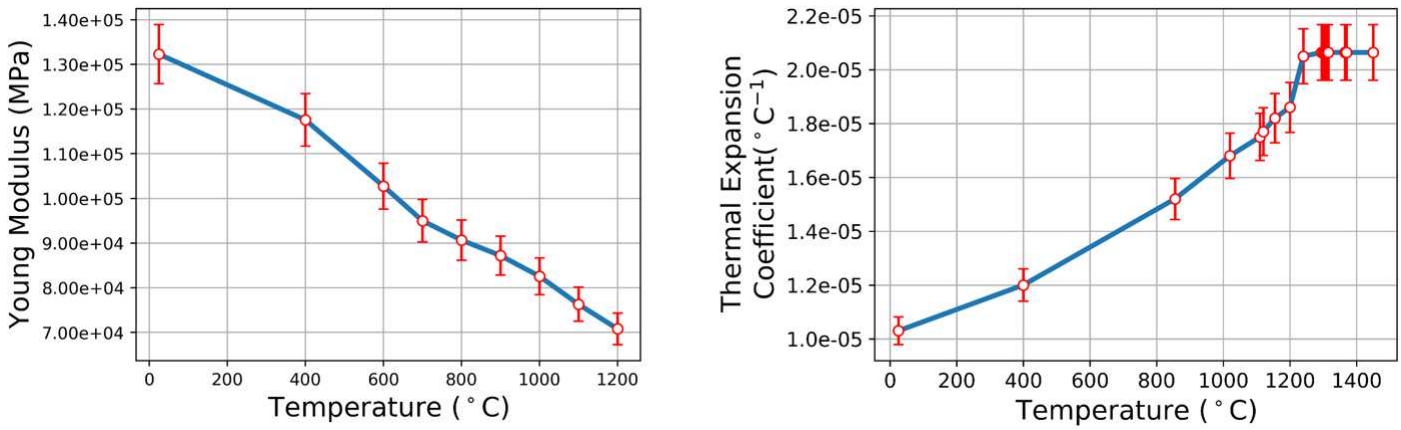


*Figure 5. Temperature evolution of Young modulus (right) and thermal expansion coefficient (left) of AM1 (courtesy of Safran Aircraft Engines).*

All previously presented data, together with Young modulus and thermal expansion (see Figure 5) coefficient evolutions with respect to temperature, are taken from an internal database, courtesy of Safran Aircraft Engines.

In the following, both isothermal and anisothermal tests performed on simple specimens are discussed. The test conditions (namely the strain rate and temperature) are chosen to be applicable to a real turbine blade casting process. Loading strain rates are $10^{-5}$ $s^{-1}$ and $10^{-3}$ $s^{-1}$ and temperature varies over a range from 25°C to 1200°C for isothermal tests, and 400 to 1200°C for anisothermal tests.

The aim of these tests is to provide sufficient data to proceed with the identification of the developed model parameters. Indeed, the identification procedure is performed for the solid phase (considering $g_S$=1) as isothermal tests cannot be ran higher than 1200°C due to technical limitations. Isothermal tests, described in details in the following, are first conducted. However, isothermal tests are not sufficient to represent all possible thermomecanical loading paths that real parts can experience during casting. Additional anisothermal tests and subsequent parameters identification are thus performed resulting in a better comparison between experimental data and numerical results. (Panisawas et al., 2013) is one of the very few works performing anisothermal tests. At the end of the tests, they analyzed the microstructure of the specimens and detected the appearance of a recrystallization phenomenon for specific temperature conditions and deformation rate.

## Isothermal tests

Multiple tests at various temperatures and strain rates are performed. The specimens used are machined from plates that have been previously cast a given production conditions. Figure 6 shows the geometry of the specimen. A tension machine equipped with an extensometer (10.0 mm of length gauge) and an induction heating system was used.

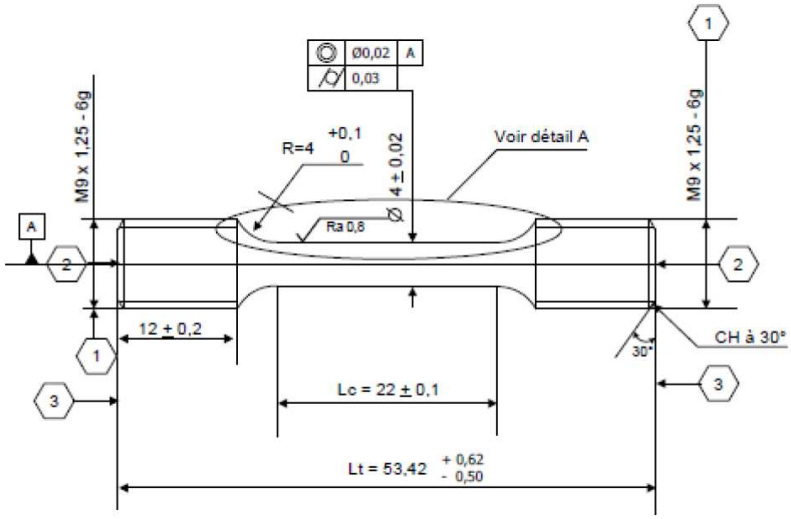


*Figure 6. Geometry and sizes of the specimen in millimeters (courtesy of Safran Aircraft Engines).*

Each test consists in a simple isothermal interrupted tensile test at fixed loading strain rate followed by a relaxation test at identical temperature (study of the evolution of stress at given constant deformation). By assessing not only the changes in stress levels for a given strain, we are able to identify the values of the multiple parameters appearing in the elasto-viscoplastic model developed above. Practically, the tensile test is first performed up to a certain strain level ε (usually 2%) prior to switching to the relaxation test during 7200 seconds. The tests are performed within several temperature values (25 °C, 400°C, 600°C, 700°C, 800°C, 900°C, 1000°C, 1100°C and 1200 °C) with a maximal strain about 2.% for a loading strain rate of $10^{-5}$ $s^{-1}$ or $10^{-3}$ $s^{-1}$. A comprehensive list of isothermal tests conditions is provided in Table 3.

Figure 7 and Figure 8 show comparisons of experimental and numerical results respectively at $10^{-5}$ $s^{-1}$ and $10^{-3}$ $s^{-1}$. In both cases, a good agreement is obtained for all temperatures, except for 700°C at $10^{-5}s^{-1}$ where the difference between the experimental curve and the numerically predicted curve is especially noticeable. We can also see that our model is able to correctly predict both stress/strain responses in the tensile phase and stress/time responses in the relaxation phase. During the cooling phase when casting a real part, a good modeling of the relaxation phase is crucial for evaluating the final stress state using numerical simulation.

| Temperature [°C] | Strain rate | Testing | Relaxation |
|---|---|---|---|
| 25°C | $10^{-3}$ $s^{-1}$ | tension up to 2% strain | 7200 seconds |
| 400°C | $10^{-3}$ $s^{-1}$ | | |
| 700°C | $10^{-3}$ $s^{-1}$ ; $10^{-5}$ $s^{-1}$ | | |
| 800°C | $10^{-3}$ $s^{-1}$ ; $10^{-5}$ $s^{-1}$ | | |
| 900°C | $10^{-3}$ $s^{-1}$ ; $10^{-5}$ $s^{-1}$ | | |
| 1000°C | $10^{-3}$ $s^{-1}$ ; $10^{-5}$ $s^{-1}$ | | |
| 1100°C | $10^{-3}$ $s^{-1}$ ; $10^{-5}$ $s^{-1}$ | | |
| 1200°C | $10^{-3}$ $s^{-1}$ ; $10^{-5}$ $s^{-1}$ | | |

*Table 3. List of isothermal tests*

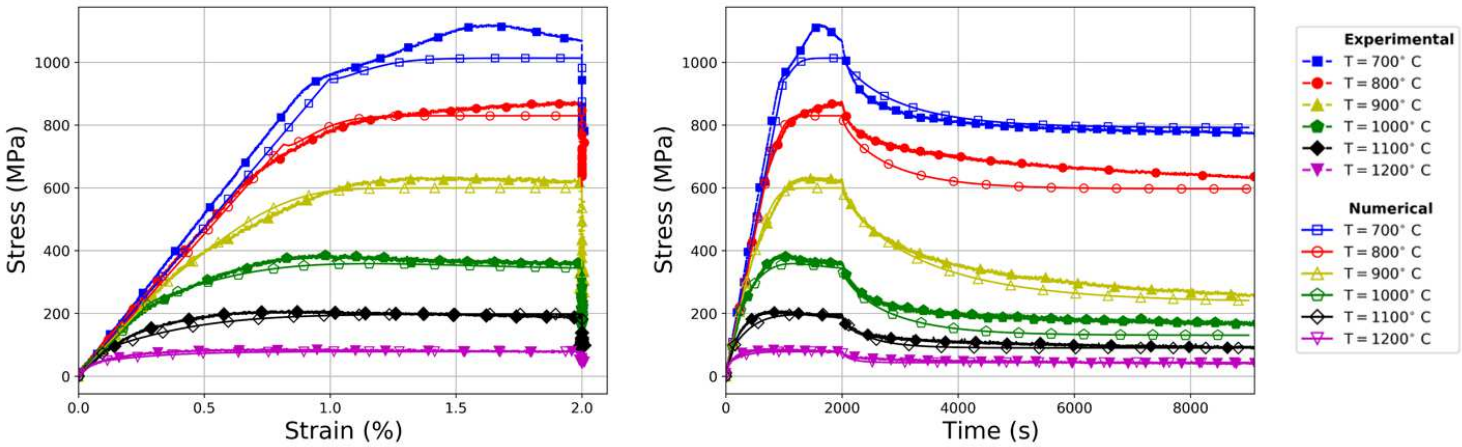


*Figure 7. Isothermal tests stress-strain (left) and stress-time (right) diagrams at $10^{-5}s^{-1}$ for various temperatures.*

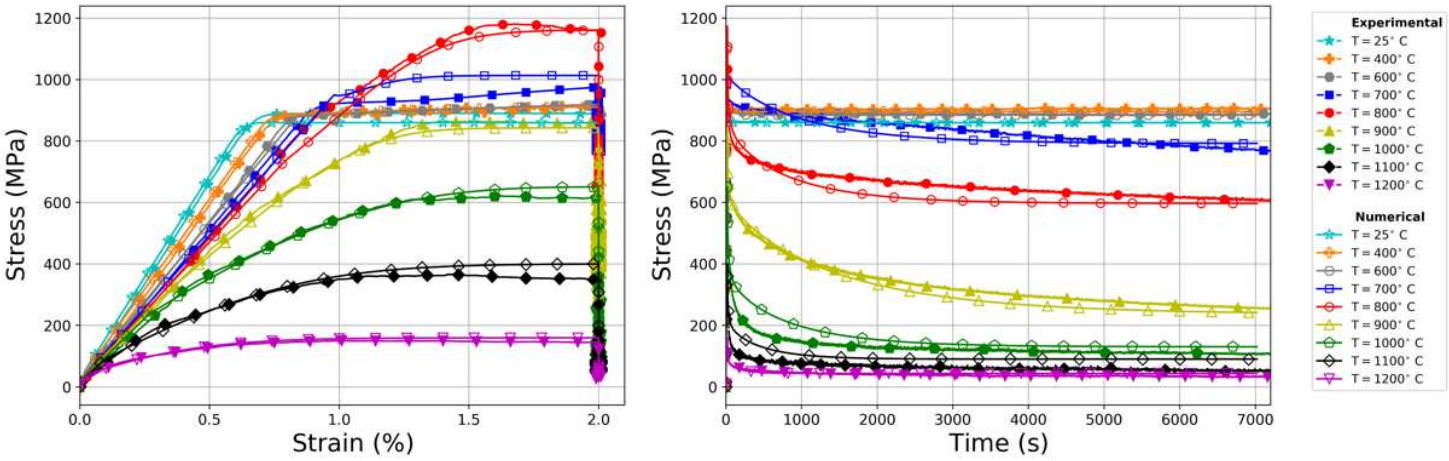


*Figure 8. Isothermal tests stress-strain (left) and stress-time (right) diagrams at $10^{-3}s^{-1}$ for various temperatures.*

One can notice that the elastic behaviour at 700°C at $10^{-5}s^{-1}$ also exhibits a slight deviation between numerical and experimental data. In order to achieve a better fit, it is possible to artificially increase the values of Young modulus implemented in our database for these isothermal simulations. Nevertheless, this deviation can be due to multiple cause from measurement uncertainty to elastic anisotropy of the real material; the latter will be investigated in future work.

It is important to recall that the identification procedure uses experimental results defined in a temperature range between $T_0$=25°C and $T_{last}$=1200°C. This temperature range does not contain the temperature corresponding to the solid-mush transition which is between $T_{coal}$ and $T_{coh}$ ($T_{coal}$=1269°C and $T_{coh}$=1300°C). To fill this lack of experimental information on the identified parameters of the model, we have used a strategy to define their evolution in this temperature domain. This strategy is obviously a first approach which is quite debatable and could be improved by additional experimental results:

- The yield stress limit $\sigma_T^e$ and viscous modulus $K_{vT}$ are kept constant at the value Tmax (if $T \geq T_{last} \rightarrow \sigma_T^e = \sigma_{T_{max}}^e$ and $K_{vT} = K_{vT_{max}}$ )
- The isotropic hardening modulus $A_T$ is linearly extrapolated with the last slope at solidus temperature $T_s$=1255°C. Between $T_s$ and $T_{coh}$ it is defined linearly decreasing towards zero (Annihilation of strain-hardening for $T \geq T_{coh} \rightarrow A_T = 0$ ).
- The hardening saturation parameter $b_T$ and $b_{vT}$ are extrapolated linearly with the last slope at the solidus temperature $T_s$ and then kept constant at the value $T_s$.

The identification methodology was therefore used to obtain the model parameters for different temperatures. Figure 9 shows the evolution of yield limit and viscosity modulus as a

function of temperature. It should be noted that the evolution of these two parameters are quite similar. We observe an increase in the yield limit over the temperature interval T∈[0°C-700°C] as well as in the viscosity modulus for the interval T∈[0°C-900°C]. These two parameters then progressively decrease. We suppose that these evolutions are governed by metallurgical transformations that we have not tried to model in this paper.

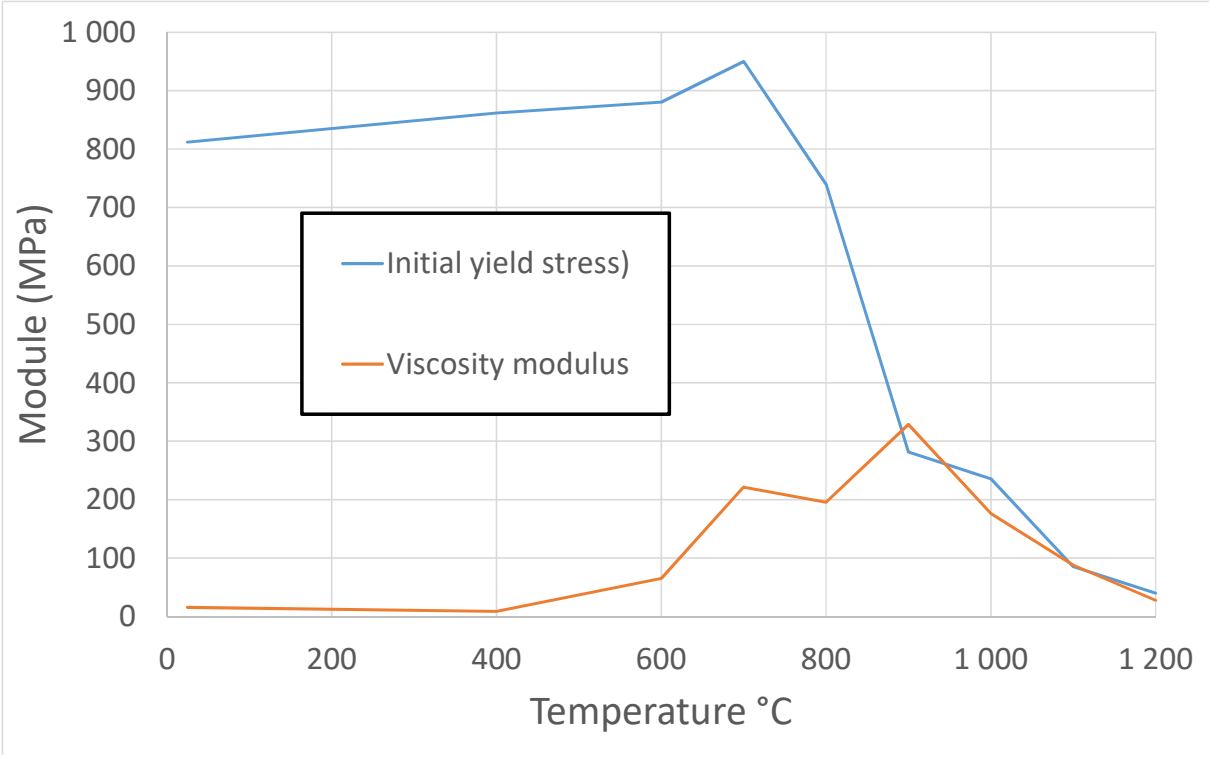


*Figure 9. Evolution of initial yield and viscosity modulus vs temperature.*

## Anisothermal tests

Anisothermal simulations are performed on a single integration point. In Figure 10, strain and temperature imposed as boundary conditions are shown. The geometry of the specimen is similar to isothermal tension-relaxation test (see back Figure 6). First, the specimen is slowly heated to a temperature of 1200°C. In the first part 0s<t<2000s, the specimen is loading to compression until a strain of (-1%) and at the same time cooled at an average cooling rate of -26°C/min. For the second part of the time 2000 s<t<5400 s, the loads are reversed, the specimen is loaded in tension and heated at an average heat rate of 13.2° C/min.

~~The evolutions of computed stress and strain components along loading direction are compared to experimental results in Figure 11, while comparison in terms of stress-strain curves is presented in . Calculated mechanical and thermal strains are plotted vs the time in Figure 12a together with corresponding strain rates (Figure 11b).~~

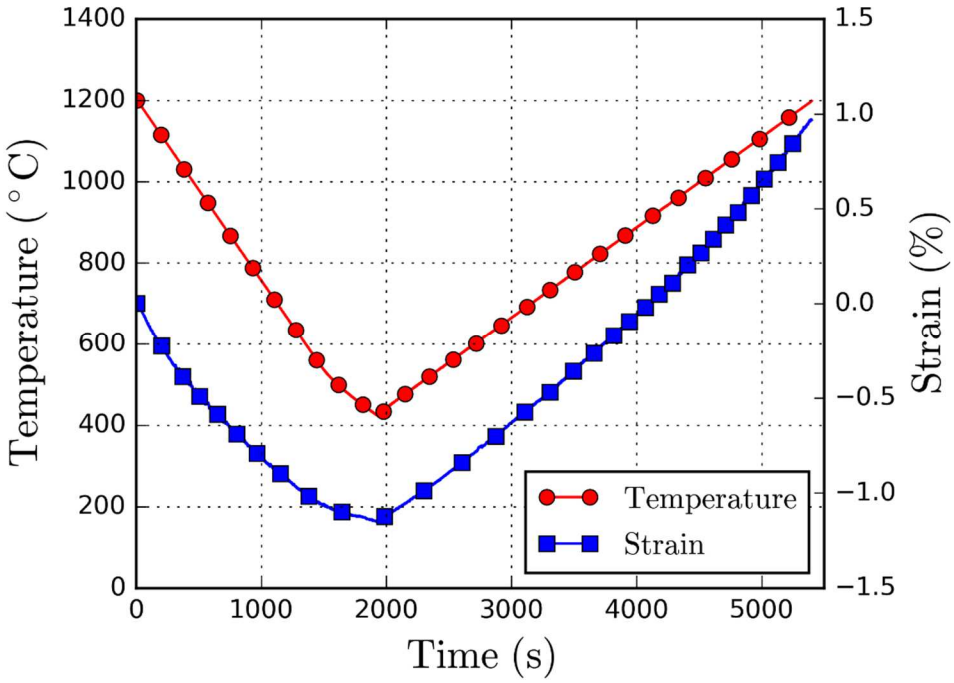


*Figure 10. Temperature and strain imposed boundary conditions during anisothermal tests.*

The stress and strain curves given in Figure 11 (a) and (b) show good fitting with experimental results, particularly the stress maximum value and the time at which it is reached are quite well predicted. Some deviation is nonetheless observed at some specific locations. First, stress grows faster in simulation than observed experimentally during the initial compression phase. Second, while experimental stress grows slower at the beginning of tensile phase between 2000 and 3500 seconds, the evolution of computed stress on the contrary seems constant.

It is worth noting that stress remains positive and still increases after switching from compression to tensile loading paths occurring at time 2000 seconds; it only starts decreasing around 3700 seconds. This feature can be explained by the differential evolutions of thermal and mechanical strains induced by imposed displacement, which govern stress direction. As observed in Figure 12, thermal strain evolves faster than mechanical strain during compression phase and slower during tensile phase. In these conditions, the specimen turns out to be in tension during the entire test as illustrated in Figure 13. Stress finally decreases, because mechanical properties of the material are altered towards viscoplasticity by the raise of temperature, as supported by Figure 14.

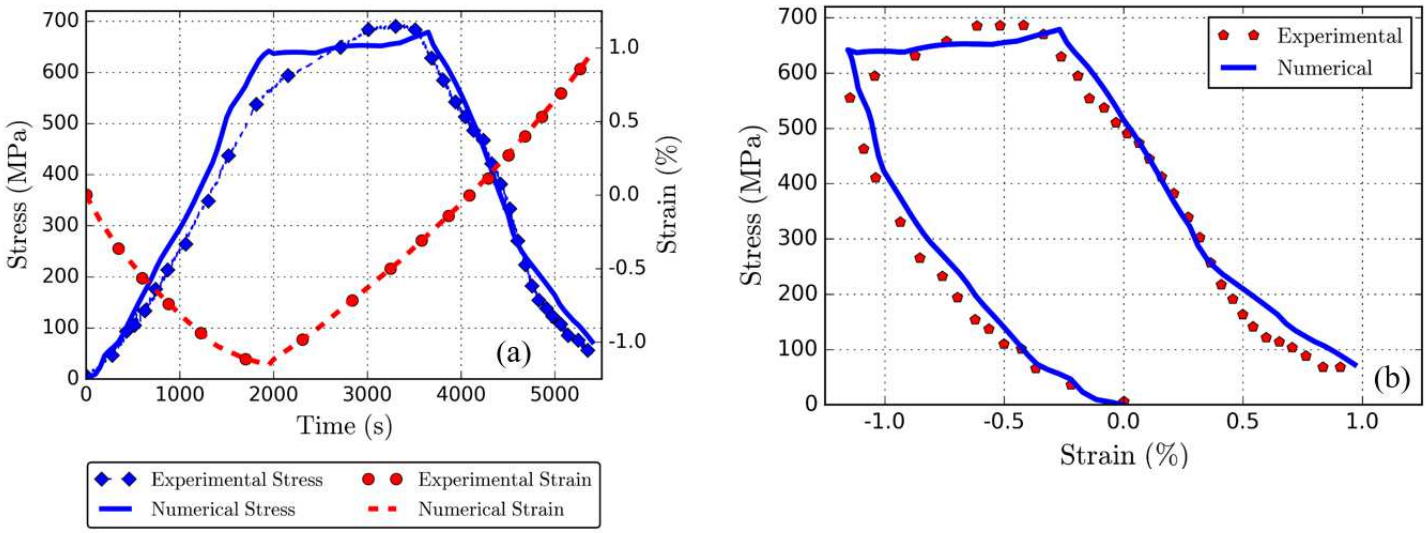


*Figure 11. (a) Time evolution of measured and computed stress and strain during anisothermal tests.(b) Anisothermal tests diagram of stress versus strain.*

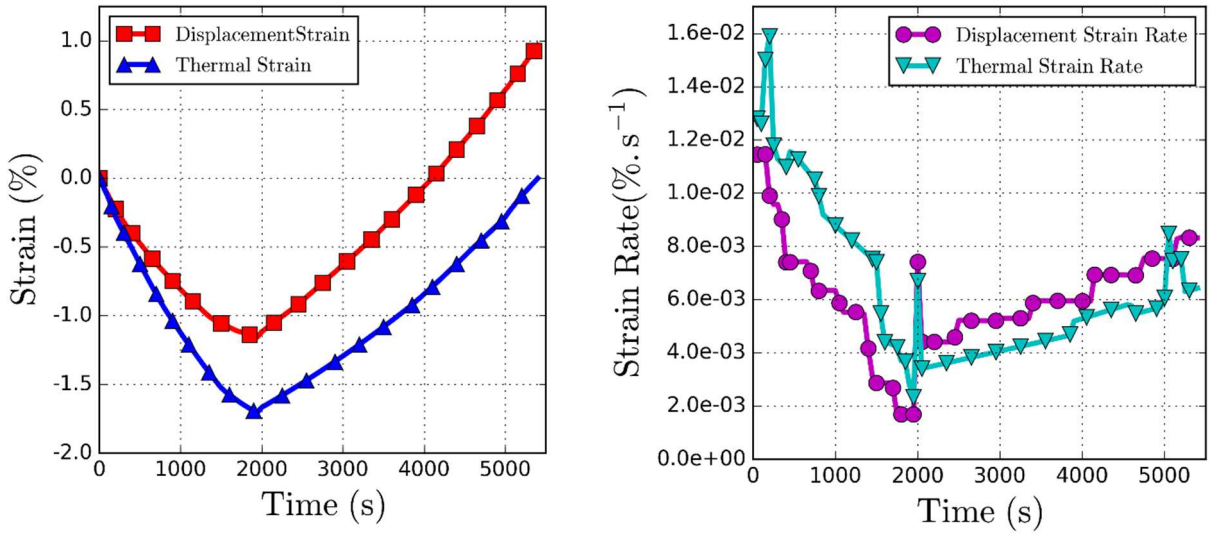


(a) (b)

*Figure 12. Time evolution of (a) displacement and thermal strains, (b) corresponding strain rates.*

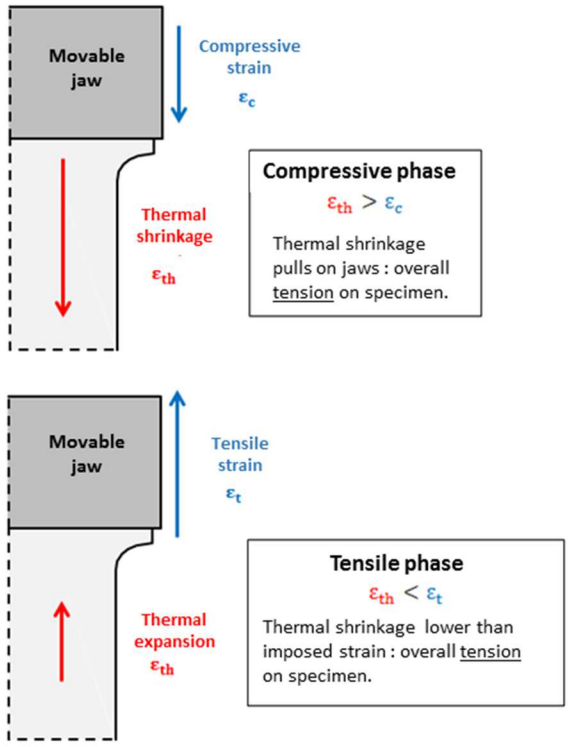


*Figure 13. Schematic representation of compressive and tensile phases. Displacement (blue) and thermal (red) strains are relatively sketched in order to show why the specimen is always in tension.*

In the latter, we first observe that from temperature 750°C to 1200°C, the identified yield stress (identified with previous isothermal tests) decreases, while it increases from 550 ° C to 750 ° C. A plateau is observed between 25 °C and 600 ° C and a maximum value is reached between 670 ° C and 770 ° C. The same singular evolution is consistent with observations presented in the work by (Caron et al., 2011). Second, Figure 14(a) suggests that plasticity occurs during the tensile phase of the test, at t > 3700s, when stress becomes greater than the corresponding yield stress at a given temperature. This is consistent with the time evolution of calculated strains, presented in Figure 14(b).

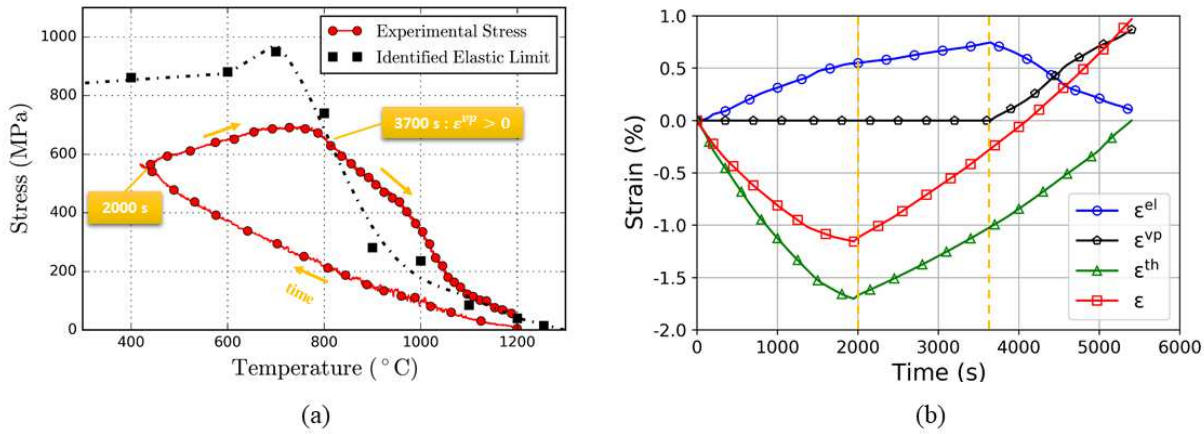


*Figure 14. (a) Comparison between the experimentally measured stress with the numerically identified yield stress. Black dashed line is a fitting curve of the yield stress. The evolution of time is indicated with yellow arrows. Plasticity occurs when stress becomes greater than the elastic limit, for instance when t > 3700 s. (b) Decomposition of total strain (red) as elastic strain (blue), plastic strain (black) and thermal strain (green) at different times. Yellow dashed lines correspond to previously marked times. For t > 3700s, plasticity occurs, which is consistent with the calculated stress state.*

Previous elements allow us to think that plastic phase is correctly predicted while the thermoelastic stage is not well described. At first sight, the observed deviation can possibly be due either to an arbitrary choice of reference temperature $T_{ref}$ when computing the thermal loading increment, or to the dispersion of the thermal expansion coefficient $\alpha_T$. For instance, in the used experiments, $T_{ref}$ can vary between 10 and 30°C, and the chosen default value is about 25°C in the previous simulations. In addition, a 5% deviation on the measurement of the thermal expansion coefficient may be accounted for.

The influence of $T_{ref}$ is first investigated. Additional simulations are carried out with $T_{ref}$ = 10, 15, 20 and 30°C. $T_{ref}$ = 25°C corresponds to the original case. Considering Figure 15, it turns out that this parameter has very little influence. This was expected as a 20°C variation only represents 5% of the process temperature at most.

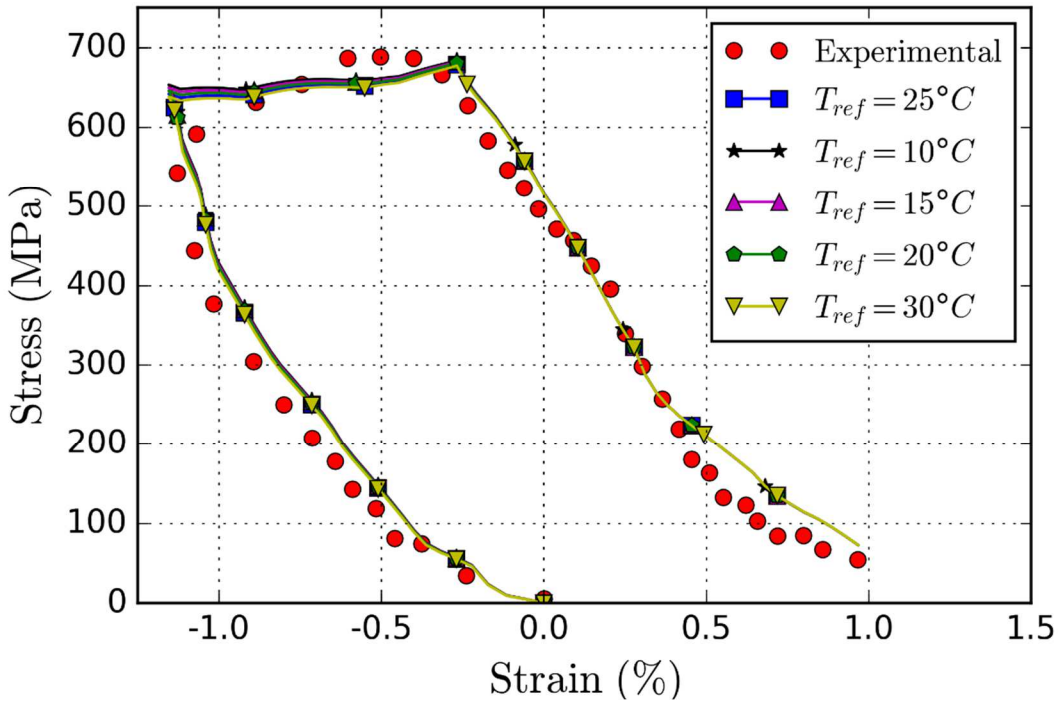


*Figure 15. Parametric study of the reference temperature $T_{ref}$. Predicted stress versus strain diagrams are plotted together with experimental data.*

Second, new simulations are performed with a scale factor $C_{scal}$ varying between 0.96 and 1.04 applied to $\alpha$. This feature is used for preliminary sensitivity tests as the simplest way to account for measurement uncertainty.

The expression of the increment of thermal displacement is hence modified as follows:

$$\Delta\varepsilon_{ij}^{th} = \left[C_{scal}\alpha_{T_{n+1}}\left(T_{n+1} - T_{ref}\right) - C_{scal}\alpha_{T_n}(T_n - T_{ref})\right]\delta_{ij} \qquad (29)$$

Results of stress versus strain are shown in Figure 16 for various values of $C_{scal}$ and showed to be much more sensitive to the latter. Corresponding computed stress errors to experimental data are summed up in Table 4.

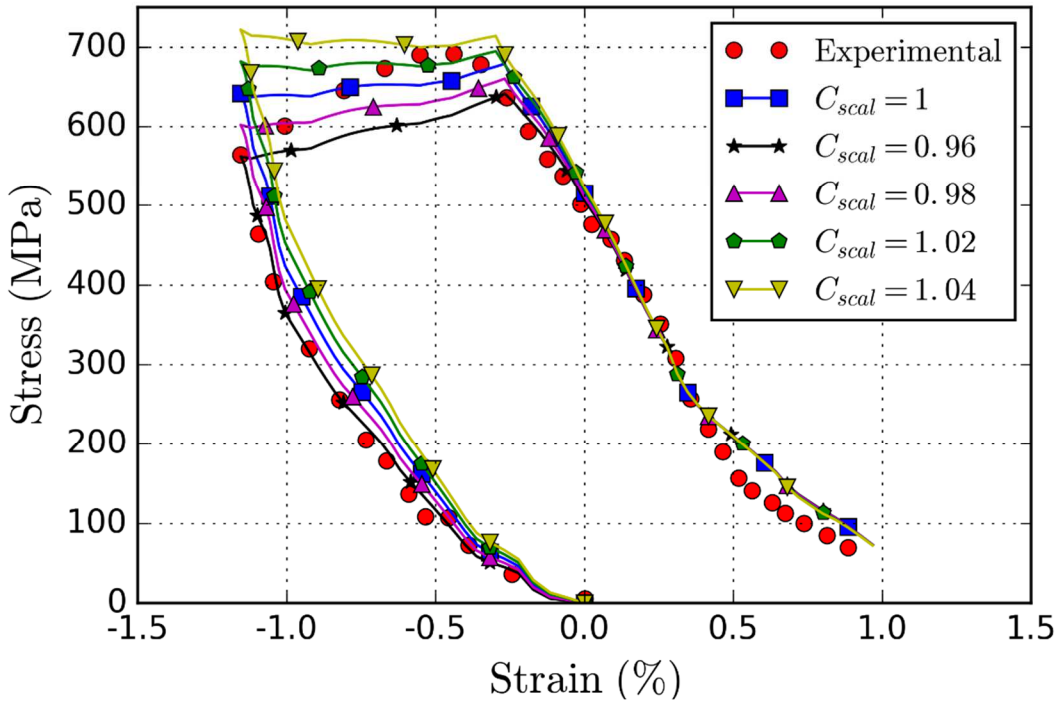


*Figure 16. Parametric study of the scaling factor $C_{scal}$. Stress versus strain diagrams are plotted together with experimental data.*

| | **Mean error (%)** | **Max error (%)** | **Min error (%)** |
|---|---|---|---|
| $\boldsymbol{C_{scal} = 1}$ | 14.9 | 94.8 | 0.08 |
| $\boldsymbol{C_{scal} = 0.96}$ | 11.6 | 96.8 | 0.15 |
| $\boldsymbol{C_{scal} = 0.98}$ | 12.5 | 95.8 | 0.35 |
| $\boldsymbol{C_{scal} = 1.02}$ | 18.4 | 93.8 | 0.05 |
| $\boldsymbol{C_{scal} = 1.04}$ | 22.4 | 92.8 | 0.20 |

*Table 4. Mean, maximal and minimal error on computed stress with respect to experimental data for various values of the scaling factor $C_{scal}$.*

The best fitting i.e. the lowest value of mean error is obtained for $C_{scal} = 0.96$. One could wisely point out that the scale factor $C_{scal}$ is here assumed constant in each simulation.

Numerical simulations with our new model have shown good agreement with experimental tests, especially during the plasticity-driven part of the tensile load. In particular, the maximal level of stress is well predicted. Deviation is mainly observed during the thermoelastic-driven

phase. The sensitivity to two main parameters, namely the reference temperature and the thermal expansion coefficient, have been investigated. The former appeared to have little influence, while the latter turned to have great influence on the numerical results. This feature has been related to the experimental measurement dispersion. Further validation tests can be led, such as determining whether plastic strain is obtained.

## 5. Finite element study of the cooling of a strained casting bar

In order to compare the developed model with classical one, in this numerical study we have considered a benchmark test involving post casting and cooling of a rectangular AM1 Ni-based superalloy bar in a sand mold. Figure 17a shows the shape and dimension of the bar. During the cooling phase, a uni-axial tensile force is applied to the right end of the bar (see Figure 17b) in order to induce mechanical strains and displacement boundary conditions are applied on the rest of bar faces.

The thermo-fluidic model and the simulation of the casting operation is done using ProCAST© FEM software. Only the cooling phase is simulated with Abaqus/Standard© software. Our numerical methodology therefore consists in deliberately decoupling the resolution of the mechanical equilibrium of the solid from the resolution of the heat equation. The evolution of the thermal field over time is simulated by ProCAST©software and then directly imposed on the model as temperature field (thermal load condition at each element of the volumic mesh). Temperature field included in the simulation is previously predicted using ProCAST© software finite element code starting from completely liquid state at 1500°C. Stress simulations are then performed using the finite element code Abaqus/Standard© (Dassault System, 2012) within the developed user material subroutine UMAT based on proposed constitutive thermo-elasto-viscoplastic model account for transition solid-liquid occurring in the media during the cooling phase.

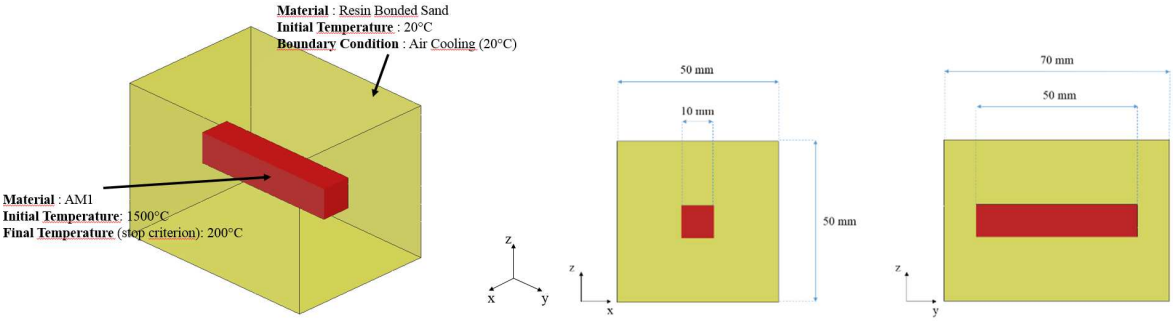


(a) benchmark test involving post casting and cooling of a rectangular AM1 Ni-based superalloy bar in a sand mold

*thermal boundary conditions*

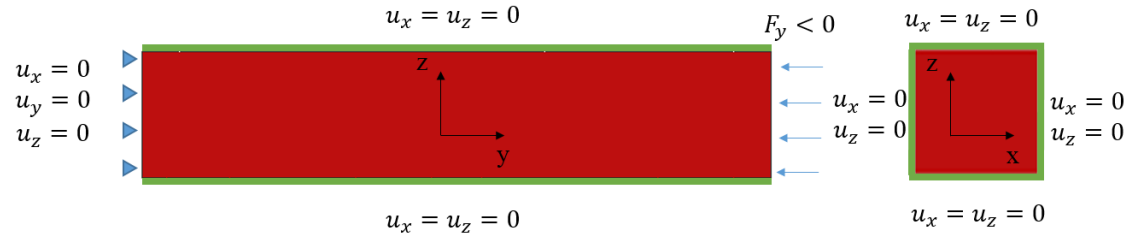


(b) mechanical boundary conditions

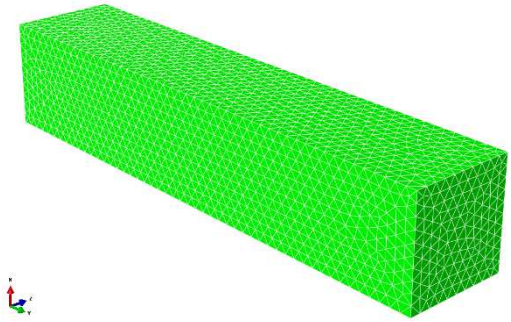

(c) Coarse mesh 51 000 elements

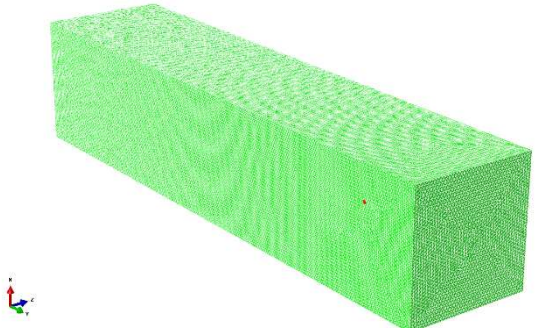

(d) Fine mesh 3 140 000 elements

*Figure 17. presentation of the benchmak test a) geometry of the bar and position of the bar in the sand mold, b) introduction of the different thermomechanical boundaries conditions c) coarse mesh of the bar d) fine mesh of the bar.*

The different thermal boundary conditions used in the PROCAST software are shown in the Figure 17a. The initial temperature of the bar is 1500°C. This bar is entirely surrounded by a temperature sand mould which is modelled by a convection flow at 20°C. The displacement boundary conditions defined in abaqus®, see Figure 17b, allow only the displacement in Y direction. A free force is applied to the right-hand end of the bar with an amplitude of Fy=0.N The bar is meshed using two sizes of 3D linear tetrahedral elements (C3D4) giving a coarse mesh composed of 510000 elements (see Figure 17c) and Fine mesh composed of 3140000 elements (see Figure 17d).

Figure 18 shows the maps of the thermal field and the solid volume fraction inside the bar for certain time steps (10s, 20s and 100s) after cooling. In this figure, we can observe that the maximum gradient of temperature is located in the center of the bar. The coldest temperatures are located inside the bar edges and bounds. We can observe that after 100s step time, the temperature in the bar varies between 806°C and 879°C for which the bar is completely solidified.

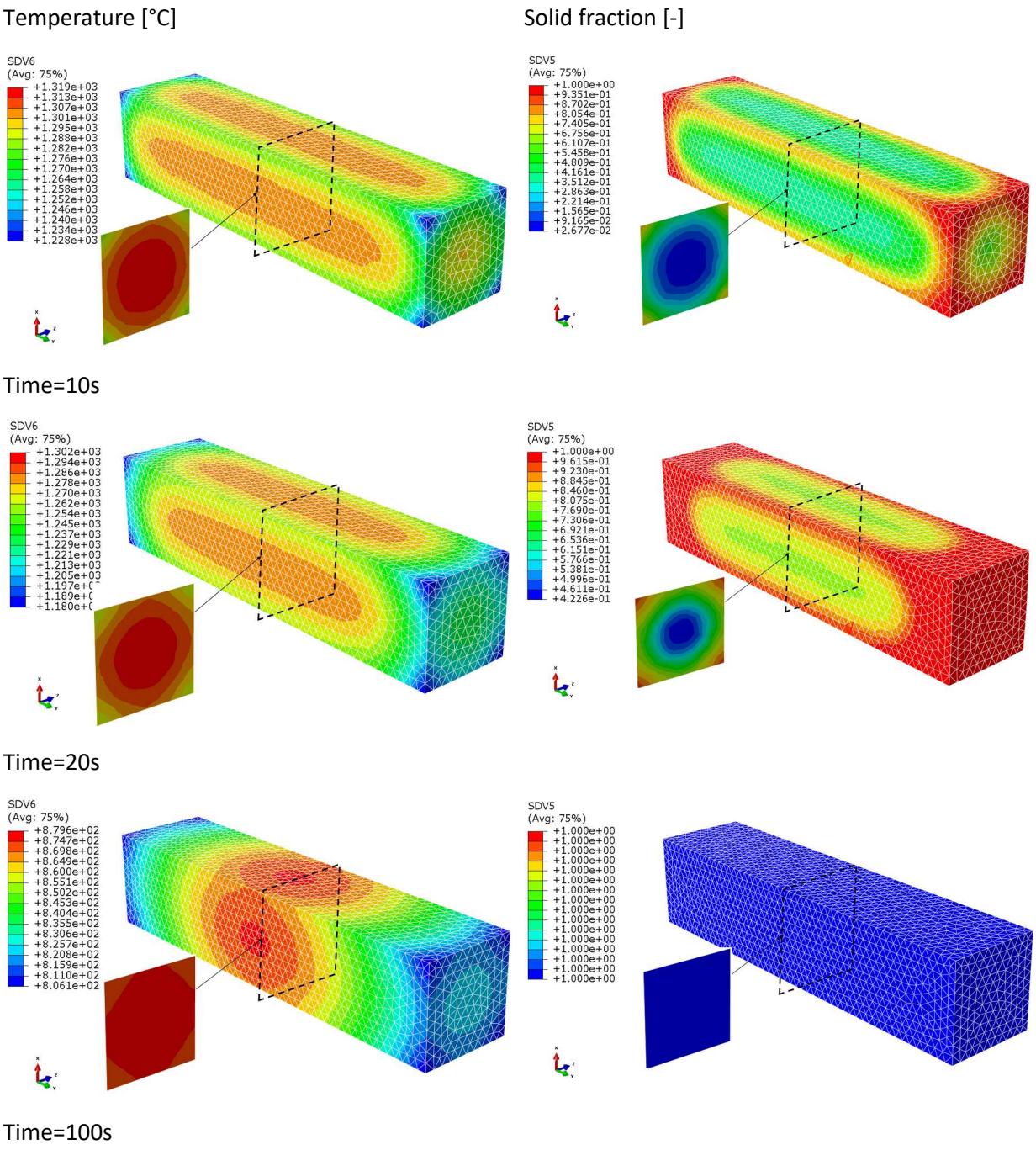


*Figure 18. Temperature and solid fraction maps for different times obtained with coarse mesh of the casting of strained bar.*

The evolution of the temperature and solid volume fraction versus time for material point-A localized in the center of the bar are plotted in Figure 19. At this point A, we can observe from the Figure 19a that the transition liquid-mushy-solid occurs over a fairly short time

interval about 25s. After 10s starts the solidification inside the bar at the point A. The evolution of the solid fraction increases monotonically and reaches $g_s$=1 after 34s.The temperature gradually drop in the bar after 5s. After 400s, the temperature becomes homogeneous inside the bar and reaches about 300°C. After 700s, the temperature decreases homogeneously to reach 200°C.

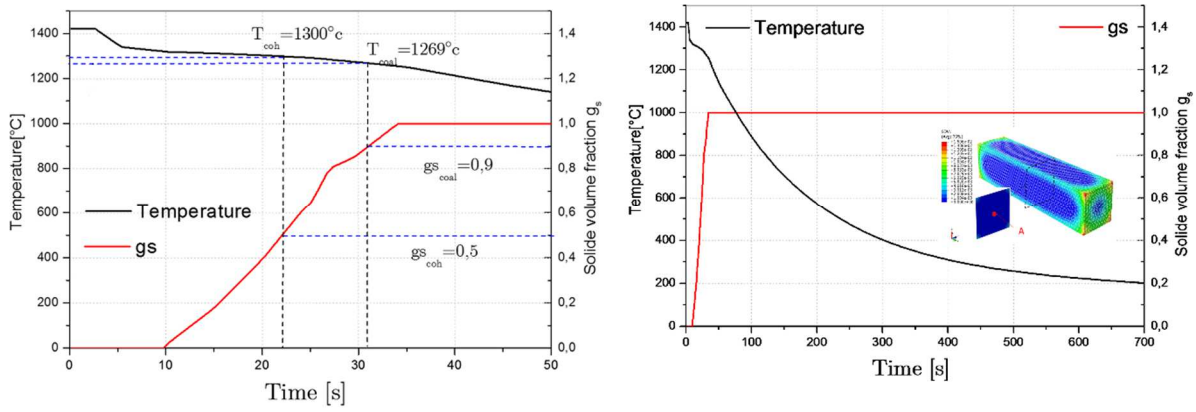


*Figure 19. Evolution of temperature and solid volume fraction vs time in the center of the bar a) zoom of the time interval t∈[0s-50s], b) plot of the time interval t∈[0s-700s]*

In the case of coarse mesh, Figure 20 shows the isovalues of von Mises stress for different time and for two cases:

- Activation of Solid-Liquid Transition (ASLT): $\forall g_s \in [0-1]$ $h_1(g_s)$, $h_2(g_s)$, $h_3(g_s)$ are defined in equation Eq.(11)
- No Activation of Solid-Liquid Transition (NASLT): $g_s = 1$ *and* $h_1(g_s) = 1$, $h_2(g_s) = 0$, $h_3(g_s) = 1$

During the solidification phase of the bar (0<t<35s), ASLT modifies slightly the von Mises stress distribution. The maximum stress is located in the corners of the bar and the minimum is concentrated in the center of the bar (where the temperature is the highest). After 100s, the distribution of von Mises stress are quite similar. The minimum and maximum are nevertheless different, 755 MPa to 909 MPa with ASLT and 780MPa to 925 MPa with NASLT. After 400s, the von Mises stress is almost homogeneous in the bar, the bar is mainly stressed in compression along the x-axis. The maximum stress level is then saturated at an average of 920 MPa. The stress distribution is then identical for ASLT or NASLT because the stress saturation level is also identical for both models.

Activation of Solid-Liquid Transition (ASLT)

No Activation of Solid-Liquid Transition (NASLT)

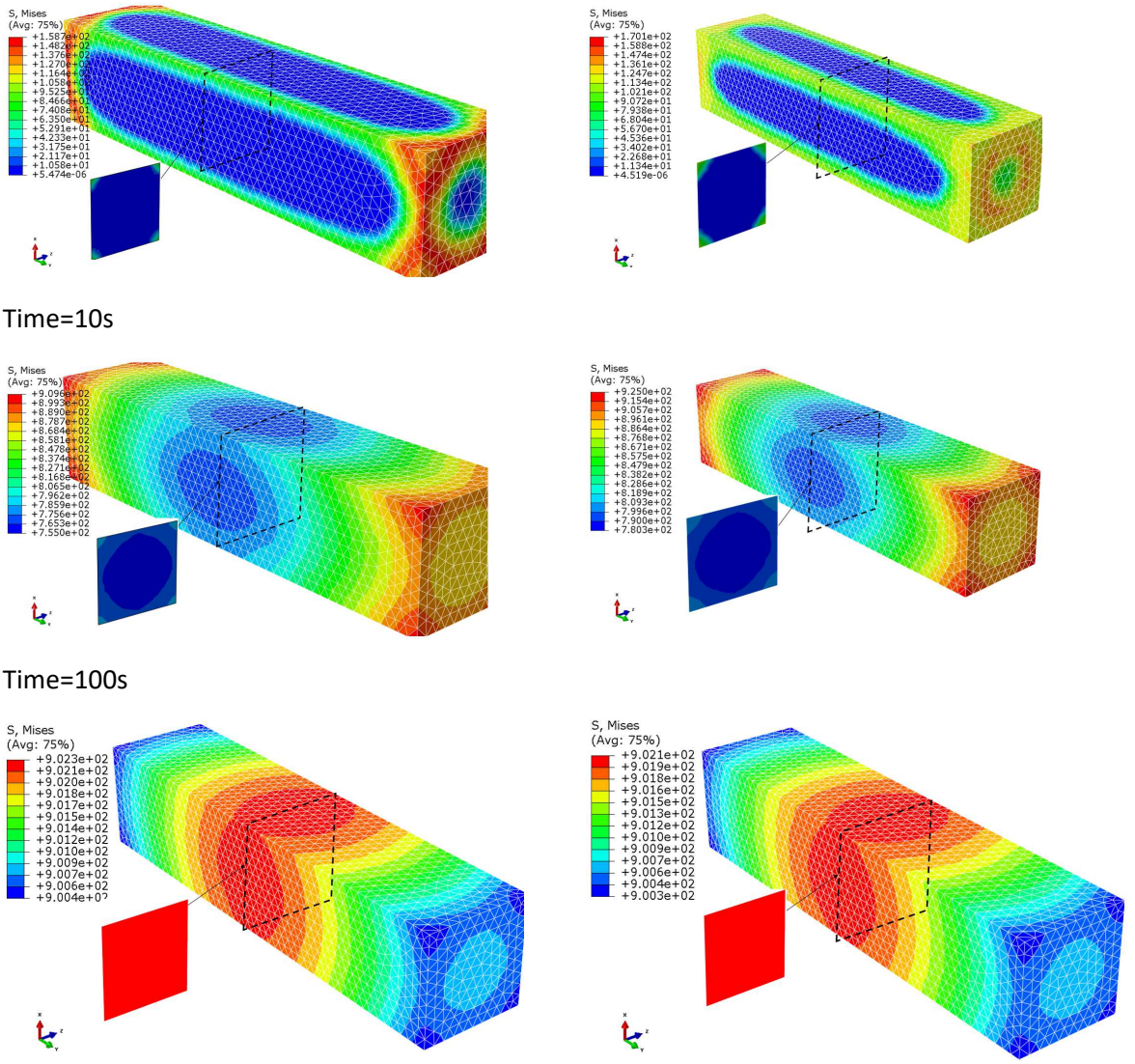


*Figure 20. Comparison between simulations of the casting of strained bar in terms of von Mises stress [in MPa] maps for at different times obtained with coarse mesh.*

Figure 21 shows the spatial distribution of accumulated plastic strain for ASLT and NASLT. We can see that ASLT generates more viscoplastic flow. During the solidification period 0<t<35s, the maximum strain is mainly located in the corners for NASLT. But for ASLT, the distribution of the plastic flow seems to be affected and the maximum is rather located along the axis of the bar. The maximum is then 0.0375 for ASLT and 0.035 for NASLT. As time passes, the difference in spatial distribution and amplitude of accumulated plastic strain between the two models (ASLT and NASLT) seems to increase. Based on the first numerical observations, we can already conclude that activation of solid-liquid transition has a significant influence on the plastic flow of the bar during its cooling. This difference necessarily generates a different plastic dissipation energy between the two models.

Activation of Solid-Liquid Transition (ASLT)

No Activation of solid-liquid transition (NASLT)

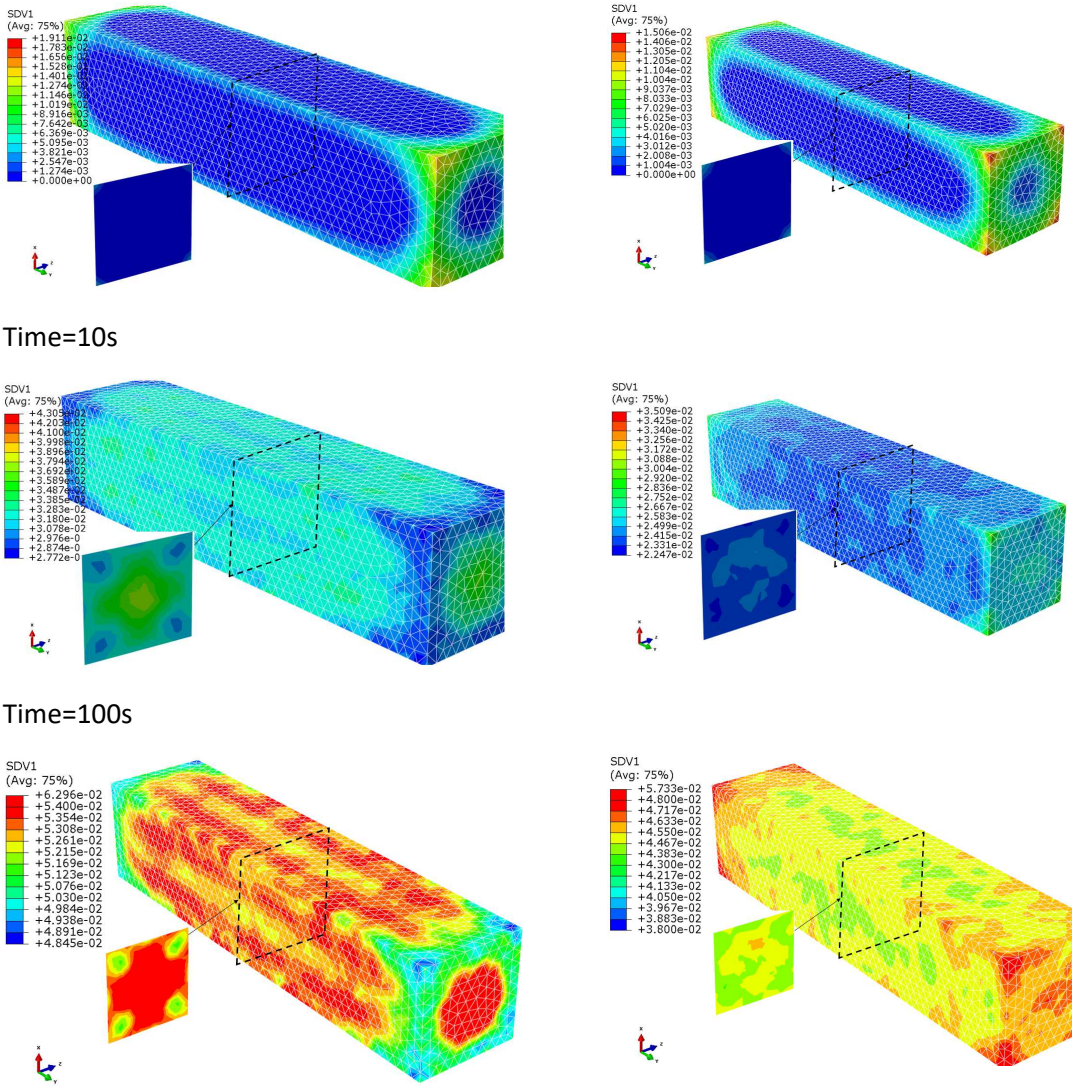


Time=10s




Time=100s




Time=400s

*Figure 21. Comparison between simulations of the casting of strained bar in terms of accumulated plastic strain maps for at different times obtained with coarse mesh.*

We will now test the sensitivity of our model to spatial discretization. Only in case ASLT, Figure 22 compares the distribution of the von Mises stress for two times (t=20s and t=400s) in the case of a coarse and fine mesh. For t=20s, we observe an identical distribution for both meshes. The fine mesh allows to better capture the areas of stress concentration but for a rather small difference (175 MPa – 173 MPa= 2 MPa). When t=400s, the two meshes give exactly the same stress distribution.

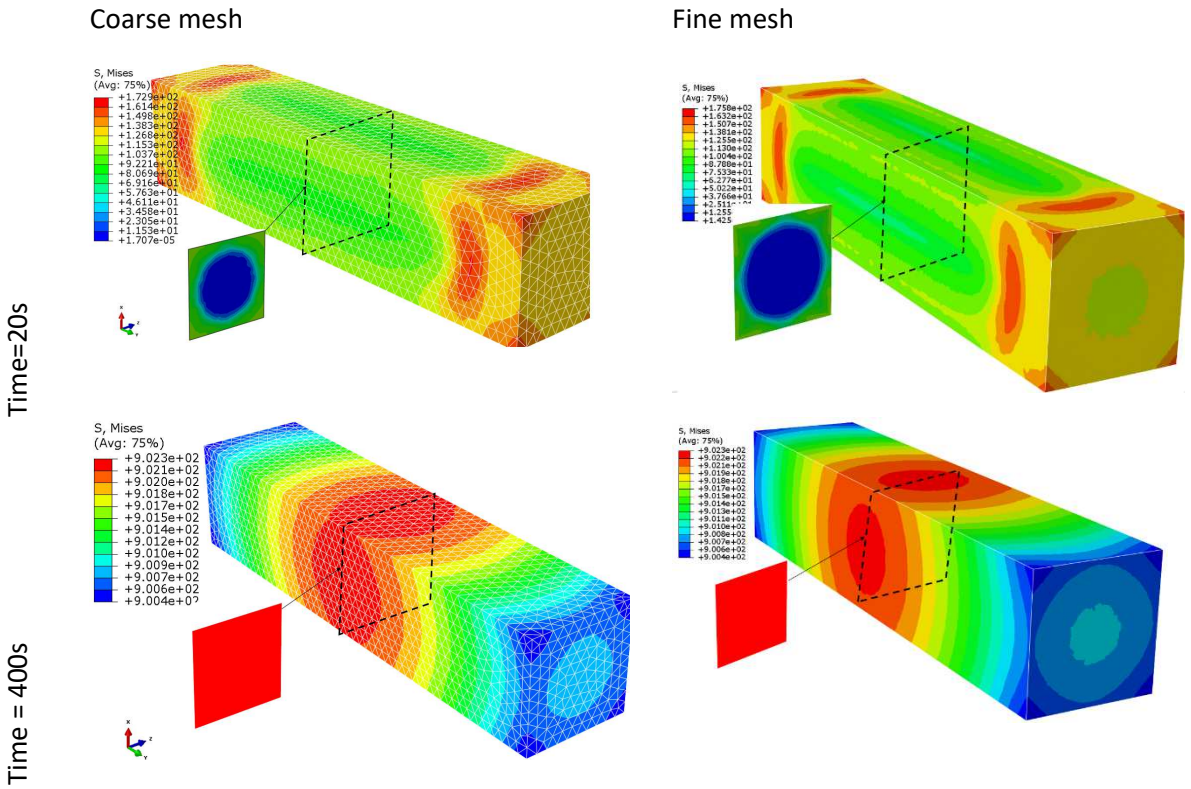


*Figure 22. Comparison of von Mises stress [in MPa] repartition between coarse and fine mesh of strained bar for two time t=20s and t=400s.*

A point in the center of the bar is selected to plot the accumulated plastic strain vs time evolution for both meshes and for ASLT and NASLT (see Figure 23). The difference in plastic flow amplitude increases very rapidly between 0<t<100s for both models (ASLT and NASLT). The difference in evolution then seems to stabilize after t>100s. After 500s, the plastic flow in the bar slows down to reach respectively at t=700s $\varepsilon_{eq}^{vp}$=0.06 for ASLT and $\varepsilon_{eq}^{vp}$=0.045 for NASLT. We can also see that the two meshes converge towards the same accumulated plastic deformation vs time evolution for case ASLT or NASLT.

Figure 23(b) shows a rather similar stress evolution between the two configurations ASLT and NASLT. However, we observe a greater difference in the cumulative plastic strain which is more important when the liquid-solid transition is activated. In parallel with this study, SAFRAN is developing a criterion based on plastic dissipation energy to predict the risk of recrystallization phenomena occurring during the solidification and cooling phase of the component (the component must keep this monocrystalline structure). We then show in this paper that the activation of the solid-mushy-liquid transition has an effect on of the plastic flow and thus on plastic dissipated energy.

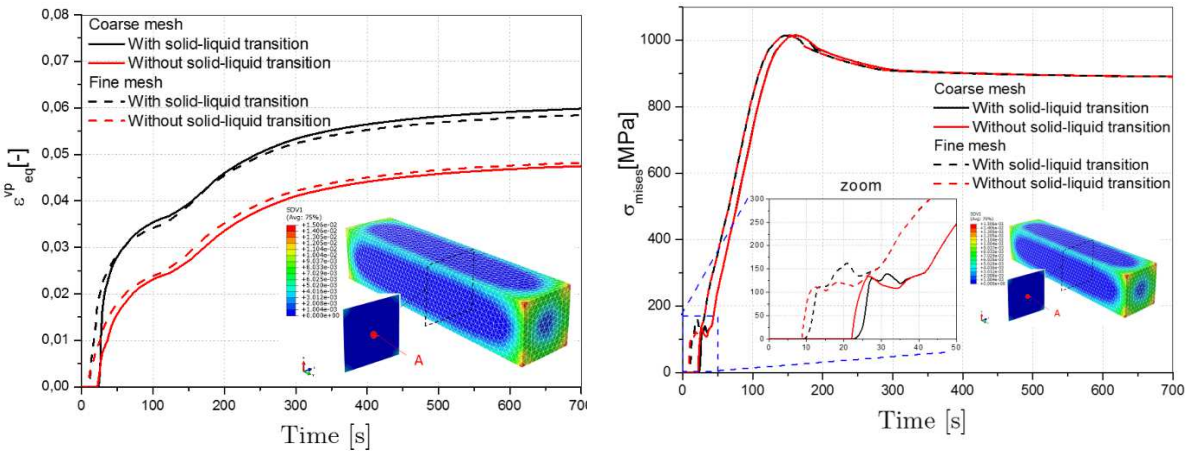


a) b)

*Figure 23. Evolution of (a) accumulated plastic strain vs time for both meshes and for ASLT and NASLT in the center of the bar, (b Mises stress vs time for both meshes and for ASLT and NASLT in the center of the bar.*

## 5. Conclusions

In this study a thermodynamically-consistent thermo-elasto-viscoplastic model was developed in order to predict the thermo-mechanical behaviour of Ni-based single crystal superalloy during its cooling phase after casting. This model takes into account the transition liquid-mushy-solid occurring in the material during the cooling phase. This is done by introducing a compressible-type viscoplastic yield function based on appropriate equivalent stress depending on volume fraction of the solid phase formed by the propagation of dendrites inside the liquid phase of the material. This model has been implemented into Abaqus/Standard© finite element code through the development of UMAT user material subroutine. An efficient identification procedure, based on multi-objective optimization methodology, has been made in order to determine all the material parameters of the model. This methodology aims to minimize the gap between the numerical and the experimental results of isothermal tensile-relaxation tests driven for different strain rates and over a large range of temperatures. A validation on anisothermal tension/compression tests has been performed. Finally, a first application has been made to parallelipipedic bar subject to solidification and cooling.

In the framework of parallepipedic bar cooling, the first conclusion is that the activation of solid-liquid modelized by a specific stress norm in the viscoplastic yield criterion increases plastic flow and thus generates more plastic dissipation energy. One of SAFRAN's main goals is to conserve a monocrystalline structure of these components during the cooling phase and after subsequent heat treatment. A criterion for detecting activation of the recrystallization phenomenon based on plastic dissipation energy is currently under study. The thermo-elasto-viscoplastic model proposed in this paper will be then coupled to this criterion in order to study the influence of the liquid-mushy-solid transition on the risk of appearance of recrystallized/hot tearing zone in the component.

However, some limitations of the proposed model have been observed and can be summarized by:

- For certain temperatures (around 700°C) and strain rate ranges, the Ni-based superalloy exhibits anomalous softening behavior that cannot be predicted by the proposed model and may be due to recrystallization phenomena which needs more advanced investigation,
- The experimental investigations are limited, due to technical constraints at a temperature range up to about 1200°C. This aspect needs additional experimental investigation in order to understand its physical meaning and enhance the capability of thermomechanical model.

## Acknowledgment

The authors wish to thank the Safran Aircraft Engines Materials and Processes Department for testing and providing experimental data used in this study. The authors would also like to thank Safran Engineering Services for supporting this study.

## References

- Pollock, T. M., & S. Tin (2006). Nickel-based superalloys for advanced turbine engines: chemistry, microstructure and properties. *Journal of propulsion and power*, *22*(2), 361-374.
- Li, Z., Xiong, J., Xu, Q., Li, J., & Liu, B. (2015). Deformation and recrystallization of single crystal nickel-based superalloys during investment casting. *Journal of Materials Processing Technology*, *217*, 1-12.
- Pokorny M.G. , Monroe C.A. , Beckermann C., Zhen Z., Hort N., (2010) "Simulation of stresses during casting of binary magnesium-aluminum, alloys", Metall. Mater. Trans. A vol 41 pp 3196–3207.
- Cocks A.C.F. (1989), "Inelastic deformation of porous materials", J. Mech. Phys. Solids, Vol. 37, n°6, pp 693-715
- Marin E.B., McDowell D.L., (1997) A semi-implicit integration scheme for rate-dependent and rate-independent plasticity, Computers & Structures, Vol 63, n°3, pp 597-600.
- D.J. Galles, C. Beckermann (2016), *In Situ Measurement and Prediction of Stresses and Strains During Casting of Steel*, Metallurgical and Materials Transactions A, Vol 47A, pp 829-848
- Bellet M., Jaouen O., Poitrault I. (2005), An ALE-FEM approach to the thermomechanics of solidification processes with application to the prediction of pipe shrinkage, Internat. J. Numer. Methods Heat Fluid Flow 15 , vol 2–3, pp 120 ALE
- Zhang S., Guillemot G., Gandin C.A., Bellet M., (2019), A partitioned two-step solution algorithm for concurrent fluid flow and stress–strain numerical simulation in solidification processes, Comput. Methods Appl. Mech. Engrg. Vol 356 pp 294–324
- Martin C.L., Favier D., Suery M., (1997) Viscoplastic behaviour of porous metallic materials saturated with liquid, Part I: constitutive equations,Int. J. Plast. Vol 13, pp 215copla
- Fedelich B., (2002), A microstructural model for the monotonic and the cyclic mechanical behavior of single crystals of superalloys at high temperatures, International Journal of Plasticity, vol18, pp 1-49

- Cruzado, A., Gan, B., Jiménez, M., Barba, D., Ostolaza, K., Linaza, A., Molina-Aldareguia, J.M., Llorca, J. & Segurado, J. (2015). Multiscale modeling of the mechanical behavior of IN718 superalloy based on micropillar compression and computational homogenization. *Acta Materialia*, *98*, 242-253.
- Cruzado, A., LLorca, J., & Segurado, J. (2017). Modeling cyclic deformation of inconel 718 superalloy by means of crystal plasticity and computational homogenization. *International Journal of Solids and Structures*, *122*, 148-161.
- Keshavarz, S., & Ghosh, S. (2013). Multi-scale crystal plasticity finite element model approach to modeling nickel-based superalloys. *Acta Materialia*, *61*(17), 6549-6561.
- Song, J.E., McDowell, D.L.: Grain scale crystal plasticity model with slip and microtwinning for a third generation Ni-base disk alloy. Superalloys 2012, 159-166 (2012)
- Michel J.C. , P. Suquet P., (1992) The constitutive law of nonlinear viscous and porous materials, J. Mech. Phys Solids, Vol 40., n°4, pp 783-812, 1992
- Përzyna P., (1966),*Fundamental problems in viscoplasticity*, Advances in Applied Mechanics, 9, pp. 343-377
- Lemaitre J., J.L. ChabocheJ.L. (1985) Mécanique des matériaux solides. Dunod, Paris, 1ème éditions.
- D. Marquardt, « An Algorithm for Least-Squares Estimation of Nonlinear Parameters », *SIAM J. Appl. Math.* **11**, 1963, p. 431-441, 1963
- Saanouni K., (2013), Damage Mechanics in Metal Forming: Advanced Modeling and Numerical Simulation, book Wiley edition,
- H. Badreddine, C. Labergere, K. Saanouni (2016)« Ductile damage prediction in sheet and bulk metal forming », *Comptes Rendus Mécanique « Computational Simulation of Manufacturing Processes »*, Vol 344, Issues 4-5, pp 296-318
- M. Issa., C. Labergere, K. Saanouni, A. Rassineux,(2012) Numerical prediction of thermomechanical field localization in orthogonal cutting, CIRP Journal of Manufacturing Science and technology, Vol 3, pp 175-195
- F. Meng , C. Labergere, P. Lafon (2014), Multi-objective optimization based on meta-models of an aeronautical hub including the ductile damage constraint, *International Journal of Damage Mechanics***,** Vol 23, pp 1055-1076
- Panwisawas, C., Mathur, H., Gebelin, J. C., Putman, D., Rae, C. M., & Reed, R. C. (2013). Prediction of recrystallization in investment cast single-crystal superalloys. *Acta Materialia*, *61*(1), 51-66.
- Caron P. Diologent F., Drawin Stefan (2011), influence of chemistry on the tensile yield strength of Nickel-based single crystal superalloys, Advanced Materials Research, Vol 278, pp 345-350
- Dassault Systèmes. (2012). ABAQUS Analysis User's Manual, Version 6.12. *Dassault Systèmes, Providence, RI*.

# Appendix n°1

Expression of the terms used in the newton Raphson algorithm for the calculation of the plastic multiplier.

The term $\partial f^{(k)}_{vp\,n+1} / \partial \Delta\varepsilon^{vp}_{eqn+1}$ is determined throw :

$$\frac{\partial f_{vp\,n+1}}{\partial \Delta\varepsilon^{vp}_{eqn+1}} = \frac{\partial \sigma^{eq}_{n+1}(\tilde{\sigma}_{ij\,n+1}, g_{sn+1})}{\partial \Delta\varepsilon^{vp}_{eqn+1}} - h_3(g_{sn+1}) \frac{\partial \sigma_{sn+1}(\varepsilon^{vp}_{eqn+1}, T_{n+1})}{\partial \Delta\varepsilon^{vp}_{eqn+1}} - h_3(g_{sn+1}) \frac{\partial \sigma_{vpn+1}(\varepsilon^{vp}_{eqn+1}, \dot{\varepsilon}^{vp}_{eqn+1}, T_{n+1})}{\partial \Delta\varepsilon^{vp}_{eqn+1}} \tag{30}$$

where :

$$\frac{\partial \sigma^{eq}_{n+1}(\tilde{\sigma}_{ij\,n+1}, g_{sn+1})}{\partial \Delta\varepsilon^{vp}_{eqn+1}} = \frac{\partial \sigma^{eq}_{n+1}}{\partial \tilde{\sigma}_{ij\,n+1}} \frac{\partial \tilde{\sigma}_{ij\,n+1}}{\partial \Delta\varepsilon^{vp}_{eqn+1}} = n_{ijn+1} \frac{\partial \tilde{\sigma}_{ij\,n+1}}{\partial \Delta\varepsilon^{vp}_{eqn+1}}$$

$$\frac{\partial \tilde{\sigma}_{ij\,n+1}}{\partial \Delta\varepsilon^{vp}_{eqn+1}} = -\frac{1}{\sigma^{eq}_{n+1}} \left[ \begin{array}{l} (1 + \dfrac{\Delta\varepsilon^{vp}_{eqn+1}}{\sigma^{eq}_{n+1}} 3\mu_e h_1)\delta_{ik}\delta_{jl} + \dfrac{\Delta\varepsilon^{vp}_{eqn+1}}{\sigma^{eq}_{n+1}} \left(K_e h_2 - \mu_e h_1\right)\delta_{ij}\delta_{kl} \\ -\dfrac{\Delta\varepsilon^{vp}_{eqn+1}}{\sigma^{eq\,2}_{n+1}} \left(3\mu_e h_1 \tilde{\sigma}^{D}_{ijn+1} + K_e h_2 tr(\tilde{\sigma}_{rs\,n+1})\delta_{ij}\right) n_{kl\,n+1} \end{array} \right] \tag{31}$$

$$\frac{\partial \sigma_{sn+1}(\varepsilon^{vp}_{eqn+1}, T_{n+1})}{\partial \Delta\varepsilon^{vp}_{eqn+1}} + \frac{\partial \sigma_{vpn+1}(\varepsilon^{vp}_{eqn+1}, \dot{\varepsilon}^{vp}_{eqn+1}, T_{n+1})}{\partial \Delta\varepsilon^{vp}_{eqn+1}} = b_{T_{n+1}} A_{T_{n+1}} Exp(-b_{T_{n+1}} \varepsilon^{vp}_{eqn+1})$$

$$+ \begin{cases} \dfrac{mK_{T_{n+1}}}{\Delta t \dot{\varepsilon}_0}(1 - Exp(-b_{vT_{n+1}} \varepsilon^{vp}_{eqn+1})) \left(\dfrac{\dot{\varepsilon}^{vp}_{eqn+1}}{\dot{\varepsilon}_0}\right)^{m_{T_{n+1}}-1} + K_{T_{n+1}} b_{vT_{n+1}} Exp(-b_{vT_{n+1}} \varepsilon^{vp}_{eqn+1}) \left(\dfrac{\dot{\varepsilon}^{vp}_{eqn+1}}{\dot{\varepsilon}_0}\right)^{m_{T_{n+1}}} & if \ \dfrac{\dot{\varepsilon}^{vp}_{eqn+1}}{\dot{\varepsilon}_0} > 1 \\ \dfrac{K_{T_{n+1}}}{\Delta t \dot{\varepsilon}_0}(1 - Exp(-b_{vT_{n+1}} \varepsilon^{vp}_{eqn+1})) \left[ 2(m-1)\dfrac{\dot{\varepsilon}^{vp}_{eqn+1}}{\dot{\varepsilon}_0} + (2-m) \right] & if \ \dfrac{\dot{\varepsilon}^{vp}_{eqn+1}}{\dot{\varepsilon}_0} \le 1 \\ \quad + K_{T_{n+1}} b_{vT_{n+1}} Exp(-b_{vT_{n+1}} \varepsilon^{vp}_{eqn+1}) \left[ (m-1)\dfrac{\dot{\varepsilon}^{vp\,2}_{eqn+1}}{\dot{\varepsilon}_0} + (2-m)\dfrac{\dot{\varepsilon}^{vp}_{eqn+1}}{\dot{\varepsilon}_0} \right] & \end{cases}$$

# Appendix n°2

Expression of the tangent operator $C_{ijkl}$ :

$$\Delta\tilde{\sigma}_{ij} = C_{ijkl}\Delta\varepsilon_{kl}$$

$$C_{ijkl} = \frac{\partial\tilde{\sigma}_{ijn+1}}{\partial\Delta\varepsilon_{kl}} = \frac{\partial\tilde{\sigma}^{*}_{ijn+1}}{\partial\Delta\varepsilon_{kl}} - \frac{\partial}{\partial\Delta\varepsilon_{kl}}\left\{\frac{\Delta\varepsilon^{eq}_{n+1}}{\sigma^{eq}_{n+1}}\left[3\mu_e h_1\tilde{\sigma}^{D}_{ijn+1} + K_e h_2 tr(\tilde{\sigma}_{kl\,n+1})\delta_{ij}\right]\right\}$$

$$C_{ijkl} = \frac{\partial\tilde{\sigma}_{ij\,n+1}}{\partial\Delta\varepsilon_{kl}} = \begin{Bmatrix} (1+\frac{\Delta\varepsilon^{eq}_{n+1}}{\sigma^{eq}_{n+1}}3\mu_e h_1)\delta_{ir}\delta_{js} + \frac{\Delta\varepsilon^{eq}_{n+1}}{\sigma^{eq}_{n+1}}(K_e h_2 - \mu_e h_1)\delta_{ij}\delta_{rs} \\ -\frac{\Delta\varepsilon^{eq}_{n+1}}{\sigma^{eq2}_{n+1}}\left[3\mu_e h_1\tilde{\sigma}^{D}_{ij\,n+1} + K_e h_2 tr(\tilde{\sigma}_{kl\,n+1})\delta_{ij}\right]n_{rs} \end{Bmatrix}^{-1}$$

$$\begin{Bmatrix} \delta_{ru}\delta_{sv} + \frac{1}{\sigma^{eq}_{n+1}\frac{\partial f_{n+1}}{\partial\Delta\varepsilon^{eq}_{n+1}}}\begin{pmatrix} 3\mu_e h_1\tilde{\sigma}^{D}_{rs\,n+1} \\ +K_e h_2 tr(\tilde{\sigma}_{mn\,n+1})\delta_{rs} \end{pmatrix}n_{uv} \end{Bmatrix} \mathrm{A}^{*}_{uvkl}$$

Note that when the increment is purely elastic, the tangent operator is reduced to :

$$C^{*}_{ijkl} = 2\mu_e(g_{sn+1}, T_{n+1})\delta_{ik}\delta_{jl} + \frac{1}{3}\left[K_e(g_{sn+1}, T_{n+1}) - 2\mu_e(g_{sn+1}, T_{n+1})\right]\delta_{ij}\delta_{kl}$$